A&A 608, A51 (2017)
DOI: 10.1051/0004-6361/201731314

Astronomy & Astrophysics

The WISSH quasars project

III. X-ray properties of hyper-luminous quasars

S. Martocchia[1,2], E. Piconcelli[2], L. Zappacosta[2], F. Duras[2,3], G. Vietri[2,4], C. Vignali[5,6], S. Bianchi[3], M. Bischetti[2,7], A. Bongiorno[2], M. Brusa[5,6], G. Lanzuisi[6], A. Marconi[8,9], S. Mathur[10], G. Miniutti[11], F. Nicastro[2], G. Bruni[12,13], and F. Fiore[2]

[1] Astrophysics Research Institute, Liverpool John Moores University, 146 Brownlow Hill, Liverpool L3 5RF, UK
e-mail: silvia.martocchia@gmail.com
[2] INAF–Osservatorio Astronomico di Roma, via Frascati 33, 00078 Monteporzio Catone, Italy
[3] Dipartimento di Matematica e Fisica, Università degli Studi Roma Tre, via della Vasca Navale 84, 00146 Roma, Italy
[4] Università degli Studi di Roma "La Sapienza", Piazzale Aldo Moro 5, 00185 Roma, Italy
[5] Dipartimento di Fisica e Astronomia, Università di Bologna, viale Berti Pichat 6/2, 40127 Bologna, Italy
[6] INAF–Osservatorio Astronomico di Bologna, via Ranzani 1, 40127 Bologna, Italy
[7] Università degli Studi di Roma "Tor Vergata", via Orazio Raimondo 18, 00173 Roma, Italy
[8] Dipartimento di Fisica e Astronomia, Università di Firenze, via G. Sansone 1, 50019 Sesto Fiorentino, Firenze, Italy
[9] INAF–Osservatorio Astrofisico di Arcetri, Largo E. Fermi 5, 50125 Firenze, Italy
[10] Ohio State University, 140 West 18th Avenue, Columbus, OH 43210, USA
[11] Centro de Astrobiología (CSIC–INTA), Depto. de Astrofísica, ESAC Campus, Camino Bajo del Castillo s/n, 28692 Villanueva de la Cañada, Spain
[12] INAF–Istituto di Astrofisica e Planetologia Spaziali, via Fosso del Cavaliere 100, 00133 Rome, Italy
[13] Max Planck Institute for Radio Astronomy, Auf dem Hugel 69, 53121 Bonn, Germany

Received 5 June 2017 / Accepted 31 July 2017

ABSTRACT

We performed a survey of the X-ray properties of 41 objects from the WISE/SDSS selected hyper-luminous (WISSH) quasars sample, which includes 86 broad-line quasars with bolometric luminosity $L_{\rm Bol} \gtrsim 2 \times 10^{47}$ erg s^{-1} shining at $z \sim 2$–4. We used both proprietary and archival *Chandra* and *XMM-Newton* observations. Twenty-one quasars have sufficient quality data to perform a spectroscopic analysis, while for the remaining sources, X-ray properties are derived through hardness-ratio analysis (apart for six sources that result to be undetected). The bulk (∼70%) of the detected WISSH quasars exhibit $N_{\rm H} < 5 \times 10^{22}$ cm^{-2}, in agreement with their optical Type 1 AGN classification. All but three quasars show unabsorbed 2–10 keV luminosities $L_{2-10} \geq 10^{45}$ erg s^{-1}. Thanks to their extreme radiative output across the mid-IR-to-X-ray range, WISSH quasars therefore offer the opportunity to significantly extend and validate the existing relations involving L_{2-10}. Specifically, we studied the X-ray luminosity as a function of (i) X-ray-to-optical (X/O) flux ratio; (ii) mid-IR luminosity ($L_{\rm MIR}$); (iii) $L_{\rm Bol}$, and (iv) $\alpha_{\rm OX}$ versus 2500 Å luminosity. We find that the WISSH quasars show (i) unreported very low X/O (<0.1) compared to typical AGN values; (ii) $L_{2-10}/L_{\rm MIR}$ ratios that are significantly smaller than those derived for AGN with lower luminosity; (iii) a large X-ray bolometric correction, $k_{\rm Bol,X} \approx 100$–1000; and (iv) steep $-2 \gtrsim \alpha_{\rm OX} \gtrsim -1.7$. These results lead to a scenario in which the X-ray emission of hyper-luminous quasars is relatively weaker compared to lower luminosity AGN. Models predict that such an X-ray weakness can be relevant for the acceleration of powerful high-ionization, emission-line-driven winds, which are commonly detected in the UV spectra of WISSH quasars and can, in turn, perturb the X-ray corona and weaken its emission. Accordingly, hyper-luminous quasars represent the ideal laboratory to study the link between the AGN energy output and wind acceleration. Additionally, WISSH quasars exhibit very large SMBH masses ($\log[M_{\rm BH}/M_\odot] \gtrsim 9.5$). This enables a more robust modeling of the Γ–$M_{\rm BH}$ relation by increasing the statistics at high masses. We derive a flatter Γ dependence than previously found over the broad range $5 \lesssim \log(M_{\rm BH}/M_\odot) \lesssim 11$. Finally, we estimate that only 300 ks observations of X-IFU on board *Athena* will offer a detailed view of the properties of absorption features associated with powerful X-ray SMBH winds for a representative sample of WISSH quasars.

Key words. galaxies: active – galaxies: nuclei – quasars: emission lines – quasars: general – quasars: supermassive black holes – techniques: imaging spectroscopy

1. Introduction

X-ray observations have been demonstrated to be a key tool to probe the nature of the innermost region of active galactic nuclei (AGN). The power-law-like spectrum of the X-ray continuum emission is interpreted as the result of Compton upscattering of thermal UV photons produced from the optically thick accretion disk surrounding the supermassive black hole (SMBH) inside an optically thin corona with an electron temperature of $kT_{\rm e} \sim$ 50–100 keV (Haardt & Maraschi 1991, 1993; Haardt et al. 1994; Petrucci et al. 2000; Reis & Miller 2013). This two-phase, disk-corona model has been supported by broadband UV-to-X-rays and ultra-hard X-ray observations (e.g., Zdziarski et al. 1996; Nandra et al. 2000; Petrucci et al. 2013), although the exact geometry and size of the corona are still largely unconstrained. Furthermore, the X-ray radiation

emitted by the corona impinging onto the underlying accretion disk and the circumnuclear gas produces the so-called reflection emission, whose bell shape peaked at ∼30 keV is the result of photo-electric absorption at low energies and Compton scattering at high energies (Ferland & Rees 1988; Matt et al. 1991). The X-ray spectral continuum in AGN can be also modified by the presence of cold and warm absorbers, located at different distances (∼0.1–100 pc) from the SMBH along our line of sight (Bianchi et al. 2012). Absorption occurring in highly ionized, high-velocity (∼a few 10^4 km s^{-1}) material very close to the accretion disk (∼100 gravitational radii) has also been revealed (Tombesi et al. 2015; King & Pounds 2015, and references therein).

Thanks to their high X-ray fluxes, local Seyfert-like AGN ($L_{\rm Bol} \sim 10^{44-45}$ erg s^{-1}) and moderately luminous quasars ($L_{\rm Bol} \sim 10^{45-46}$ erg s^{-1}) have been typically targeted by X-ray facilities, and our knowledge about the origin of the X-ray continuum and the physical and spectral properties of the X-ray emitting and absorbing regions in AGN have been basically derived by observations of these classes of sources (Reynolds 1997; Nandra et al. 1997; Piconcelli et al. 2005; Turner & Miller 2009). On the contrary, there have been fewer investigations of the properties of the X-ray emission and absorption in quasars at the tip of the luminosity scale (and hence, rare), which typically shine at $z > 2$, owing to their low number density and because these studies require time-consuming observations.

A fundamental improvement in the study of the luminous ($L_{\rm Bol} \sim 10^{46-47}$ erg s^{-1}) and hyper-luminous ($L_{\rm Bol} > 10^{47}$ erg s^{-1}) quasars in the ∼0.3–10 keV band have been provided by *XMM-Newton* and *Chandra* thanks to their high sensitivity and angular resolution. Both survey programs and targeted observations have been successful in providing unprecedented constraints on X-ray spectral and evolutionary properties of these powerful AGN, i.e., both unobscured and obscured AGN (see Vignali et al. 2003, 2010; Page et al. 2004; La Franca et al. 2005; Just et al. 2007; Bianchi et al. 2007; Shemmer et al. 2008; Young et al. 2009; Reeves et al. 2009; Piconcelli et al. 2015).

It has emerged that the slope of the X-ray continuum does not show strong dependence on redshift or luminosity (Nanni et al. 2017 and references therein). On the contrary, it has been found that the intensity of the reflection features in the spectra of luminous quasars is weak compared to AGN at lower luminosities (e.g., Reeves & Turner 2000; Jiménez-Bailón et al. 2005; Bianchi et al. 2007; Zappacosta et al. 2017). In addition, many studies report that the UV-to-X-ray spectral energy distribution (typically described by the relationship between the 2500 Å and 2 keV monochromatic luminosities, i.e., $\alpha_{\rm OX}$) depends primarily upon the UV luminosity (Avni & Tananbaum 1982; Vignali et al. 2003; Steffen et al. 2006; Lusso et al. 2010; Lusso & Risaliti 2016), while the redshift dependence is weak. These results lend support to a scenario whereby the mechanism responsible for the primary continuum emission in AGN remains almost identical from $z \approx 0$ to $z \approx 6$, while the more the AGN luminosity increases, the less the energy in the X-ray band is emitted relative to that in the UV-optical range. More recently, some works have reported that the X-ray to mid-infrared (MIR) luminosity relation shows a different behavior from low-to-high MIR luminosity AGN. Specifically, the ratio between X-ray and MIR luminosity is smaller for MIR luminous ($\geq 10^{46}$ erg s^{-1}) objects (Lanzuisi et al. 2009; Stern 2015).

A comprehensive investigation of nuclear properties of hyper-luminous quasars is also important for our understanding of the outflows launching mechanism and, hence, AGN-galaxy self-regulated growth. Many models indicate that an intense radiation field should be able to accelerate winds out from the immediate vicinity of the AGN accretion disk (Murray et al. 1995; Proga 2005; King & Pounds 2003) via line driving and radiation pressure. A low X-ray illumination of the outflowing gas is necessary to avoid the suppression of UV line driving by over-ionization, and explains the large blueshifts (>2000 km s^{-1}) of the CIV emission line observed in the most luminous quasars (i.e., the so-called wind-dominated quasar population; e.g., Richards et al. 2011). Furthermore, the relation between AGN luminosity and wind terminal velocity observed for broad ($FWHM \sim 10^3$ km s^{-1}) absorption line (BAL) quasars can indeed be easily accounted for by a radiatively driven outflow (Laor & Brandt 2002). Brandt et al. (2000) found that the equivalent width of the CIV BALs anticorrelates with the $\alpha_{\rm OX}$, indicating a strong link between powerful winds and soft X-ray weakness in quasars. It has been also reported that objects typically showing strong outflows, i.e., BAL quasars and AGN-dominated ultra-luminous IR galaxies (ULIRGs; Sturm et al. 2011; Cicone et al. 2014) are indeed X-ray weak compared to normal quasars (Imanishi & Terashima 2004; Sabra & Hamann 2001). The X-ray spectrum of BAL quasars and ULIRGs typically shows large obscuration and the X-ray absorbing medium has been considered the main cause for a reduced X-ray emission and very steep $\alpha_{\rm OX}$ values (e.g., Green & Mathur 1996; Mathur et al. 2000; Gallagher et al. 2002; Piconcelli et al. 2005). The X-ray absorber can also shield the BAL clouds from the ionizing continuum (Kaastra et al. 2014). Remarkably, even taking into account the measured X-ray absorption, a large percentage of BAL quasars still remain X-ray weak (Gibson et al. 2008; Luo et al. 2013), i.e., they are unable to produce strong X-ray emission. The prototype of such a class of intrinsically weak quasar is Mrk 231 for which a recent *NuSTAR* observation has confirmed the intrinsic X-ray weakness (Teng et al. 2014).

Such X-ray weakness is also a typical feature observed in the so-called weak emission line quasars (i.e., objects showing Lyα and CIV emission with an equivalent width $EW \leq 10$ Å) and quasars with highly blueshifted (>2000 km s^{-1}) CIV emission lines (e.g., Wu et al. 2012).

In this paper, we present the X-ray spectral properties of the WISE-SDSS selected hyper-luminous (WISSH) quasars sample and report on the correlations between the X-ray and multiwavelength (optical, UV and MIR) properties. The WISSH quasars project consists of a multiband (from millimeter wavelengths up to hard X-rays) investigation of 86 hyper-luminous ($L_{\rm Bol} \geq 2 \times 10^{47}$ erg s^{-1}), broad-line quasars at $z \sim 1.8-4.8$. This sample was obtained by cross-correlating the WISE All-Sky source catalog (for 22 μm flux density $S_\nu(22\ \mu{\rm m}) > 3$ mJy) and the SDSS DR7 quasar catalog (for $1.5 < z < 5$). We refer to Bischetti et al. (2017) for a detailed description of the WISSH quasar sample and the main goals of this multiband project aimed at performing a systematic study of the nuclear, outflows, and host galaxy properties of the most powerful quasars. This paper has been organized as follows. Details about X-ray observations of the sources in the WISSH sample, data reduction, and source detection are presented in Sect. 2. In Sect. 3 we present the results of the X-ray data analysis and we discuss the X-ray properties of the WISSH sample. In Sect. 4 we report on the correlation of X-ray versus optical and MIR properties, while in Sect. 5 results on X-ray bolometric corrections and relations involving SMBH mass and Eddington ratio have been outlined. In Sect. 6.1 we summarize our results and discuss the relative X-ray weakness of WISSH quasars compared to AGN at lower luminosities. We outline and conclude about possible future perspectives for the WISSH project with *Athena* X-ray observatory in Sect. 6.2.

A ΛCDM cosmology with $\Omega_\Lambda = 0.73$, $\Omega_M = 0.27$ and $H_0 = 70\ \mathrm{km\,s^{-1}}$ is assumed throughout. Hereafter, errors correspond to 1σ while upper limits are reported at 90% confidence level, unless specified otherwise.

2. X-ray observations

2.1. X-ray coverage of the WISSH sample

The X-ray sample of WISSH quasars (X-WISSH, hereafter) consists of 41 objects observed with *Chandra* or *XMM-Newton*, corresponding to 48% of X-ray coverage for the WISSH sample. Table 1 provides information about sources in the X-WISSH sample and X-ray observations (34 observations by *Chandra* and 7 by *XMM-Newton*). All sources but J1328+5818 (*XMM-Newton* Obs. ID. 0405690501) were the principal targets of the observations. We used 33 archival and 8 proprietary observations. The latter represent 20% of the sample (namely, J0209-0005, J0735+2659, J0801+5210, J1111+1336, and J1513+0855 with *Chandra* ACIS-S and J0904+1309, J1549+1245, and J2123-0050 with *XMM-Newton*). These sources are indicated with a cross in Col. 4 in Table 1.

2.2. Data reduction and source detection

Chandra data were reduced and analyzed with the *Chandra* Interactive Analysis of Observations CIAO 4.7 package[1] with CALDB 4.7.0 by standard procedures following the CIAO *Science Threads*. For each source, we created an image in the 0.5–8 keV energy band from the event file by using the `dmcopy` tool. In order to extract source and background counts, we used a circular region centered on the SDSS source position with radii between 2″ and 6″. For the background regions, we usually considered an annulus centered on the source position with inner radius ranging from 2″ to 7″ and outer radius ≥30″. However, in some cases a circular aperture (radius ≥20–30″) close to the source position was preferred to avoid contamination from nearby X-ray sources. Net counts were extracted via the `dmextract` task. Errors at 1σ confidence level were estimated either according to the Gaussian statistics for large number of counts ($N \gtrsim 20$) or according to the Gehrels approximation for lower number of counts ($1\sigma = 1 + \sqrt{N + 0.75}$; Gehrels 1986). However, the corresponding lower limit ($1\sigma = \sqrt{N - 0.25}$) is smaller and `dmextract` adopts the larger error to be conservative. Using Poisson statistics, we then calculated the false-positive probability to establish the robustness of the X-ray detection. We found that six sources (i.e., ∼15% of X-WISSH) were undetected, according to a probability threshold of 10^{-5}. A 90% upper limit on count rate was assumed for these sources.

For the quasars observed with *XMM-Newton*, the data reduction was carried out with Science Analysis System SAS[2] software package, 14.0.0 version. The EPIC *pn* Observation Data Files (ODFs) were processed with the `epproc` task to generate the event files. These files were filtered to remove flaring background periods. We applied the standard methods described in the SAS threads. Accordingly, we extracted light curves in the 10–12 keV range to exclude intervals contaminated by high-energy particles background. Good time interval (GTI) tables were then generated by setting rates less than 0.4 cts/s (RATE ≤ 0.4). The cleaned event file was created for energies extending from 0.3 keV up to 10 keV. Counts were extracted with a circular aperture with radii of ∼20–30″ (∼70–100″) for the source (background) region. Table 1 reports net counts in the 0.5–8.0 keV band with corresponding uncertainties.

[1] See http://cxc.harvard.edu/ciao
[2] See http://xmm.esac.esa.int/sas/

3. Results of X-ray analysis

3.1. Hardness ratio analysis

As a first step, we performed the hardness ratio (HR) analysis for the 35 detected sources to make inferences about the basic X-ray emission properties of these quasars.

We created images in the soft (0.5–2 keV) and hard (2–8 keV) bands from each source event file and we extracted net counts with relative uncertainties in each band as in Sect. 2.2. The HR compares the number of counts obtained in two or more energy bands. We specifically used the following definition of hardness ratio:

$$HR = \frac{H - S}{H + S}, \tag{1}$$

where H is the number of counts in the hard band and S is the number of counts in the soft band.

A power-law model with photon index $\Gamma = 1.8$ modified by intrinsic absorption with $5 \times 10^{21} \leq N_H \leq 10^{24}\ \mathrm{cm^{-2}}$ was assumed to simulate the spectrum of our sources with WebPIMMS[3]. The lower value of $N_H = 5 \times 10^{21}\ \mathrm{cm^{-2}}$ was set by the $z \gtrsim 2$ of our sources, for which the photoelectric cut-off falls outside the energy range of our observations. Specifically, we used *Chandra* WebPIMMS[4], provided by the *Chandra* Data Center, as it allows the specification of the observation cycle for *Chandra* data, taking into account the decreasing quality of the ACIS detector caused by piled-up dust over time.

This analysis revealed that the majority of the sources (∼90% of the X-WISSH) have negative HR values, suggesting little absorption in the X-rays. Indeed, by comparing the HR values with the simulated absorbed power-law models, we were able to constrain the N_H values and we found that the bulk of the objects are consistent with $N_H \leq 5 \times 10^{22}\ \mathrm{cm^{-2}}$. In Table 2 we report the HR-based N_H values except for the sources with best available data for which X-ray spectroscopic analysis was performed (see Sect. 3.2). In case of a value of HR corresponding to a N_H that is consistent within uncertainties with $5 \times 10^{21}\ \mathrm{cm^{-2}}$, we list the N_H value as 90% upper limit. To estimate X-ray fluxes, we used WebPIMMS by assuming an absorbed power law with $\Gamma = 1.8$ and N_H corresponding to the estimated HR value (see Table 2). For J1157+1337 and J1236+6554, which had upper limits on HR, we used $5 \times 10^{21}\ \mathrm{cm^{-2}}$ to derive their fluxes and luminosities. Table 2 also lists the unabsorbed 2–10 keV luminosity (L_{2-10} hereafter).

Finally, for the six undetected sources (see Sect. 2.2), we assumed a N_H equal to the maximum value of the sample, i.e., $N_H = 4 \times 10^{23}\ \mathrm{cm^{-2}}$, to derive conservative values for X-ray fluxes and luminosities.

3.2. X-ray spectroscopy

We performed X-ray spectroscopy for the 21 sources in the X-WISSH sample detected with ≥40 net counts. We created the redistribution matrix file (RMF) and auxiliary response file (ARF), using `mkacisrmf` and `mkarf` CIAO tools for *Chandra*

[3] See https://heasarc.gsfc.nasa.gov/cgi-bin/Tools/w3pimms/w3pimms.pl
[4] See http://cxc.harvard.edu/toolkit/pimms.jsp

Table 1. X-ray WISSH sample and log of the X-ray observations.

SDSS (1)	z (2)	i (3)	X-ray obs. (4)	Obs. ID (5)	Obs. date (6)	Exp (ks) (7)	Net counts (8)	$N_{\rm H}^{\rm Gal}$ (9)	Log $\lambda L_{6\ \mu{\rm m}}$ (10)
J0045+1438^{B}	1.992^{a}	16.99	*Chandra*	6889	2006-07-24	11.5	10.9 ± 3.6	5.27	46.96
J0209-0005	2.856^{a}	16.99	*Chandra*†	17078	2014-11-18	29.7	146.2 ± 12.3	2.32	47.09
J0735+2659	1.982^{a}	16.14	*Chandra*†	17077	2015-10-02	24.7	187.3 ± 13.8	4.87	47.07
J0745+4734	3.225^{b}	16.29	*Chandra*	1330	2012-01-01	1.5	81.4 ± 9.1	5.76	47.31
J0747+2739	4.11^{a}	17.91	*Chandra*	3561	2002-12-03	5.0	21.5 ± 4.7	3.66	46.83
J0801+5210	3.263^{b}	16.76	*Chandra*†	17081	2014-12-11	43.5	173.5 ± 13.4	4.32	47.20
J0900+4215	3.294^{b}	16.69	*Chandra*	6810	2006-02-09	3.9	109.6 ± 10.5	1.23	47.26
J0904+1309	2.974^{a}	17.04	XMM†	0745010301	2014-11-24	24.6	1330.6 ± 38.7	2.83	47.32
J0947+1421	3.04^{a}	17.01	*Chandra*	13325	2012-05-28	1.6	4.8 ± 3.0	3.05	47.05
J1014+4300	3.126^{a}	16.38	*Chandra*	6809	2006-06-14	4.1	33.5 ± 5.8	1.34	47.16
J1027+3543	3.112^{a}	16.59	*Chandra*	13312	2012-04-02	1.6	26.8 ± 5.2	0.99	47.40
J1057+4555	4.14^{a}	17.29	*Chandra*	878	2000-06-14	2.9	27.5 ± 5.3	0.90	47.24
J1106+6400	2.22^{b}	15.98	*Chandra*	6811	2006-07-16	3.65	123.5 ± 11.1	1.05	47.08
J1110+4831	2.957^{a}	16.55	XMM	0104861001	2002-06-01	26.8	425.5 ± 22.0	1.73	47.27
J1111+1336	3.492^{b}	17.18	*Chandra*†	17082	2015-01-26	43.1	180.7 ± 13.6	1.48	47.07
J1159+1337	3.984^{a}	17.56	*Chandra*	13323	2012-06-29	1.6	2.9 ± 1.7	2.26	47.12
J1200+3126	2.993^{a}	16.36	*Chandra*	13309	2012-03-18	1.5	15.8 ± 4.0	1.64	47.15
J1201+0116	3.247^{b}	17.32	*Chandra*	13345	2012-02-10	1.6	≤5.4	1.76	47.07
J1201+1206	3.512^{b}	17.31	*Chandra*	13324	2012-06-11	1.6	15.8 ± 4.0	1.81	47.10
J1210+1741^{B}	3.64^{a}	17.73	*Chandra*	13366	2012-07-09	1.6	≤2.5	2.83	47.16
J1215-0034^{B}	2.707^{a}	17.13	*Chandra*	4201	2003-11-14	44.5	137.7 ± 11.8	1.95	47.08
J1236+6554	3.424^{b}	17.19	*Chandra*	6817	2006-08-29	4.1	20.5 ± 4.8	1.71	47.03
J1245+0105^{B}	2.798^{a}	18.12	*Chandra*	2974	2002-05-03	6.7	10.4 ± 3.3	1.52	46.88
J1249-0159	3.638^{a}	17.73	*Chandra*	13335	2011-12-03	1.6	3.8 ± 2.0	1.61	47.01
J1250+2631	2.044^{a}	15.37	XMM	0143150201	2003-06-18	18.6	3099.6 ± 56.8	0.86	47.22
J1328+5818^{B}	3.133^{a}	18.57	XMM	0405690501	2006-11-25	43.1	34.3 ± 8.9	1.58	46.83
J1333+1649	2.089^{a}	15.99	*Chandra*	867	2000-04-03	3.0	159.6 ± 12.6	1.66	47.06
J1421+4633	3.454^{b}	17.22	*Chandra*	12859	2011-06-20	23.6	51.2 ± 7.3	1.12	47.04
J1422+4417	3.647^{b}	17.57	*Chandra*	13360	2011-11-11	1.5	≤2.5	1.01	47.38
J1426+6025	3.189^{a}	16.23	XMM	0402070101	2006-11-12	5.8	181.9 ± 14.4	1.74	47.43
J1433+0227	4.62^{a}	18.33	*Chandra*	3959	2003-04-20	3.5	≤3.8	2.59	47.02
J1441+0454	2.059^{a}	17.08	*Chandra*	12860	2012-02-28	21.5	78.2 ± 8.9	2.75	46.80
J1506+5220^{B}	4.068^{a}	18.29	*Chandra*	4071	2012-10-24	4.9	≤5.1	1.85	47.09
J1513+0855^{B}	2.897^{a}	17.09	*Chandra*†	17079	2016-04-06	29.7	298.0 ± 17.4	2.84	47.30
J1521+5202	2.218^{b}	15.44	*Chandra*	15334	2013-10-22	37.4	87.5 ± 9.5	1.58	47.22
J1538+0855	3.564^{b}	17.00	*Chandra*	13314	2012-05-02	1.6	≤2.5	3.06	47.16
J1549+1245^{B}	2.365^{b}	17.38	XMM†	0763160201	2016-02-04	30.4	520.6 ± 32.4	3.47	47.14
J1621-0042	3.71^{a}	17.26	*Chandra*	2184	2001-09-05	1.6	27.6 ± 5.3	6.59	47.08
J1639+2824^{B}	3.801^{a}	17.21	*Chandra*	13315	2011-11-24	1.5	5.8 ± 2.4	3.24	47.52
J1701+6412	2.737^{a}	15.84	*Chandra*	9756	2007-11-14	32.3	214.4 ± 14.7	2.28	47.32
J2123-0050	2.283^{b}	16.34	XMM†	0745010401	2014-11-14	21.9	785.2 ± 30.4	3.84	47.05

Notes. Columns give the following information: (1) SDSS ID; (2) redshift; (3) SDSS AB magnitudes in the i band; (4) X-ray observatory; (5) observation ID; (6) date of the X-ray observation; (7) net exposure time in ks; (8) net counts in the 0.5–8.0 keV band; (9) Galactic absorption by Kalberla et al. (2005) (in units of 10^{20} cm^{-2}); and (10) rest-frame 6 μm luminosities from Duras et al. (2017) (in units of Log[L/erg s^{-1}]). B: BAL quasars according to the modified absorption index (AI_{1000} > 100; Bruni et al. 2012), which is a more conservative version of the Hall et al. (2002) definition. The detailed analysis of the BAL properties of WISSH quasars will be presented in a forthcoming paper (Bruni et al., in prep.). ^{a} Redshifts from the SDSS DR10 catalog. ^{b} Redshifts from LBT-LUCI near-IR spectroscopy (Vietri et al., in prep.). † Proprietary data observations.

sources and `rmfgen` and `arfgen` SAS tools for XMM sources. We extracted the spectra with the same source and background regions used for the counts estimation (Sect. 2.2). In fitting the spectra using `XSPEC v.12.8.2`, we consistently applied the Cash statistics to all spectra (Cash 1979), which is more appropriate for low-count spectra. Accordingly, we rebinned the source plus background spectra to ensure that at least one count is included in each spectral bin. Spectra collected with *Chandra* (*XMM-Newton*) were fitted in the 0.3–8 (0.3–10) keV band.

A first characterization of the continuum shape of these sources was obtained by fitting each spectrum with a simple model consisting of a power law plus Galactic absorption (denominated PL model hereafter). The majority of the sources exhibit photon index close to $\Gamma \sim 1.8$, which is the typical value for a broad-line quasar (Piconcelli et al. 2005). However, eight sources show a flat photon index ($\Gamma \leq 1.5$) that is likely due to the presence of intrinsic $N_{\rm H}$ not accounted for in the PL model. We then fitted each spectrum by adding an

Table 2. X-ray properties of the WISSH quasars.

SDSS (1)	Γ (2)	$N_{\rm H}$ (3)	f_{2-10} (4)	Log L_{2-10} (5)	Model (6)	X/O (7)	$\alpha_{\rm OX}$ (8)
J0045+1438	1.8^{f}	$\leq 22(4)^{b}$	0.69	44.24	APL*	0.3	−2.21
J0209-0005	$1.25^{+0.15}_{-0.15}$	≤1.6	5.25	45.16	PL	2.3	−1.98
J0735+2659	$1.54^{+0.13}_{-0.13}$	≤3.6	7.08	45.11	PL	1.4	−1.89
J0745+4734	$1.83^{+0.18}_{-0.18}$	≤3.5	30.9	46.37	PL	7.2	−1.54
J0747+2739	1.8^{f}	$\leq 30(4)^{b}$	2.13	45.43	APL*	2.2	−1.72
J0801+5210	$1.81^{+0.14}_{-0.13}$	≤0.8	2.66	45.25	PL	1.0	−1.95
J0900+4215	$1.8^{+0.16}_{-0.15}$	≤2.3	13.5	46.00	PL	4.5	−1.66
J0904+1309	$2.05^{+0.04}_{-0.04}$	≤0.8	9.04	45.89	PL	4.2	−1.66
J0947+1421	1.8^{f}	$\leq 16(0.5)^{b}$	1.61	45.01	APL*	0.7	−1.94
J1014+4300	$1.74^{+0.32}_{-0.30}$	≤3.3	3.55	45.43	PL	0.9	−1.91
J1027+3543	1.8^{f}	$\leq 14(1)^{b}$	9.16	45.79	APL*	2.8	−1.74
J1057+4555	1.8^{f}	$\leq 17(4)^{b}$	4.62	45.77	APL*	2.7	−1.70
J1106+6400	$2.04^{+0.15}_{-0.15}$	≤0.7	12.3	45.69	PL	2.2	−1.70
J1110+4831	$1.97^{+0.08}_{-0.08}$	≤0.8	3.17	45.36	PL	0.9	−1.85
J1111+1336	$1.78^{+0.13}_{-0.13}$	≤5.7	2.61	45.36	PL	1.4	−1.85
J1159+1337	1.8^{f}	≤0.5	0.91^{c}	45.04	APL*	0.7	−1.99
J1200+3126	1.8^{f}	$\leq 15(1)^{b}$	5.78	45.55	APL*	1.4	−1.71
J1201+0116	1.8^{f}	$40^{\dagger}$	$\leq 4.21^{\ddagger}$	$\leq 45.54^{\ddagger}$	–	≤2.5	≥−1.75
J1201+1206	1.8^{f}	$\leq 44(7)^{b}$	6.60	45.77	APL*	3.9	−1.68
J1210+1741	1.8^{f}	$40^{\dagger}$	$\leq 1.72^{\ddagger}$	$\leq 45.25^{\ddagger}$	–	≤1.5	≥−1.91
J1215-0034	$1.61^{+0.34}_{-0.33}$	$21.8^{+9.2}_{-8.3}$	5.25	45.33	APL	2.6	−1.62
J1236+6554	1.8^{f}	≤0.5	2.55^{c}	45.33	APL*	1.4	−1.86
J1245+0105	1.8^{f}	30^{+20}_{-22}	1.84	45.03	APL*	2.3	−1.80
J1249-0159	1.8^{f}	$\leq 56(1)^{b}$	1.25	45.08	APL*	1.1	−1.89
J1250+2631	$2.35^{+0.07}_{-0.07}$	≤0.3	29.9	45.94	PL^{a}	3.0	−1.55
J1328+5818	1.8^{f}	30^{+40}_{-20}	2.19	45.22	APL*	4.2	−1.77
J1333+1649	1.8^{f}	$0.7^{+0.3}_{-0.2}$	25.7	45.83	APL	4.6	−1.62
J1421+4633	1.8^{f}	$13.3^{+6.2}_{-5.5}$	1.72	45.18	APL	0.9	−1.79
J1422+4417	1.8^{f}	$40^{\dagger}$	$\leq 1.84^{\ddagger}$	$\leq 45.28^{\ddagger}$	–	≤1.4	≥−1.98
J1426+6025	$1.79^{+0.13}_{-0.13}$	≤0.8	7.76	45.72	PL	1.7	−1.83
J1433+0227	1.8^{f}	$40^{\dagger}$	$\leq 0.97^{\ddagger}$	$\leq 45.22^{\ddagger}$	–	≤1.5	≥−1.86
J1441+0454	$1.7^{+0.3}_{-0.3}$	$2.7^{+2.2}_{-1.6}$	2.95	44.84	APL	1.4	−1.85
J1506+5220	1.8^{f}	$40^{\dagger}$	$\leq 1.05^{\ddagger}$	$\leq 45.14^{\ddagger}$	–	≤1.5	≥−1.92
J1513+0855	$1.71^{+0.11}_{-0.11}$	≤13.4	7.94	45.60	PL	3.9	−1.85
J1521+5202	$1.4^{+0.4}_{-0.4}$	$10.1^{+6.7}_{-6.2}$	3.52	44.85	APL	0.4	−2.02
J1538+0855	1.8^{f}	$40^{\dagger}$	$\leq 1.75^{\ddagger}$	$\leq 45.24^{\ddagger}$	–	≤0.8	≥−1.91
J1549+1245	$2.13^{+0.22}_{-0.19}$	$4.9^{+1.6}_{-1.3}$	3.98	45.34	APL	2.5	−1.83
J1621-0042	1.8^{f}	10^{+20}_{-9}	10.7	46.04	APL*	6.1	−1.58
J1639+2824	1.8^{f}	40^{+60}_{-35}	4.08	45.67	APL*	2.2	−1.87
J1701+6412	$2.18^{+0.23}_{-0.22}$	$4.3^{+2.5}_{-2.3}$	6.61	45.75	APL	1.0	−1.67
J2123-0050	$1.71^{+0.06}_{-0.05}$	≤0.4	9.16	45.43	PL	2.2	−1.80

Notes. Columns give the following information: (1) SDSS name; (2) X-ray photon index; (3) absorption $N_{\rm H}$ (in units of 10^{22} cm^{-2}); (4) 2–10 keV fluxes (in units of 10^{-14} erg cm^{-2} s^{-1}); (5) 2–10 keV unabsorbed luminosities (in units of Log[L/erg s^{-1}]); (6) hard X-ray fluxes and luminosities were derived by using the $N_{\rm H}$ value from HR and Γ = 1.8 or from spectral analysis (models: PL = power law, APL = absorbed power law); (7) X-ray-to-optical flux ratios (X/O) in units of 10^{-2}; and (8) $\alpha_{\rm OX}$ values. * Based on HR analysis. f: frozen value. [a] Best-fit model consists of a power law plus cold reflection component. [b] Value shown in parentheses indicates the $N_{\rm H}$ inferred from the HR computed with the measured soft and hard fluxes. See Sect. 3.1 for further details. [c] Flux derived by assuming the upper limit value on $N_{\rm H}$. † X-ray undetected sources. $N_{\rm H}$ = 4×10^{23} cm^{-2} is assumed. ‡ For the calculation of fluxes and luminosities, the upper limit on count rates listed in Table 1 is assumed.

extra absorption component to the PL model (named APL hereafter). We found that for 13 out of 21 sources, i.e., ∼60% of the X-ray spectral sample, the PL model provides a reasonable fit to the spectra, while the presence of an extra absorption component is required by the data for seven WISSH quasars. For two sources, namely J1333+1649 and J1421+4633, fitting with the APL model yielded an upper limit on $N_{\rm H}$ and the resulting Γ remained flat (∼1.5) and, therefore, we fixed the photon index to the canonical AGN value of Γ = 1.8. From the spectral analysis, it emerged that the majority of the sources show little or no

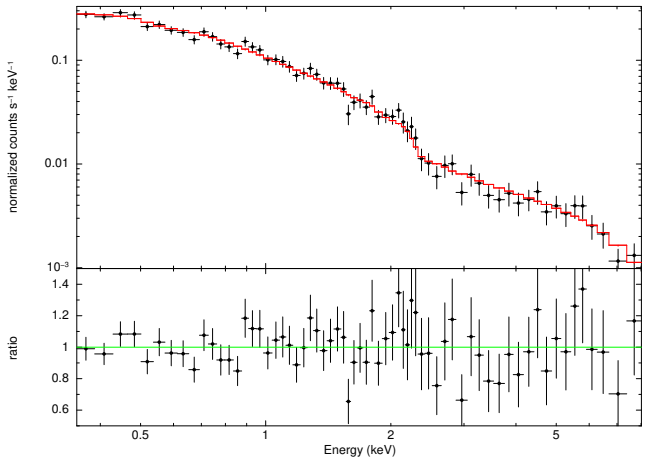

Fig. 1. *XMM-Newton* spectrum (black points) of J1250+2631 when the model PL+reflection (red solid line) is applied. *Lower panel*: data-to-model ratios.

intrinsic absorption, with 14 out of 21 quasars exhibiting a value of $N_{\rm H}$ < few 10^{22} cm^{-2}. Finally, the $N_{\rm H}$ values inferred from the spectral analysis are consistent with those based on HR.

We discuss here the peculiar case of J1250+2631, which showed additional spectral complexity with respect to PL and APL models. The *XMM-Newton* spectrum of J1250+2631 showed an evident excess at high energies when fitted with a PL model. As the observed spectral range (0.3–10 keV) corresponds to a rest-frame energy range of ~0.9–30 keV, we added a Compton reflection component to account for this excess using `pexrav` (Magdziarz & Zdziarski 1995). A cut-off energy of E = 300 keV was fixed, metal abundances were set to solar values, and the inclination angle of the reflector cos(i) = 0.45. Thus, we were able to fit both the reflected and intrinsic continuum X-ray emission, whose slope results to be steep ($\Gamma = 2.35^{+0.12}_{-0.10}$). This model provides the best description of the spectrum of J1250+2631 (see Fig. 1), with an associated Cstat/d.o.f. = 45/60, compared to the Cstat/d.o.f. = 69/61 derived by the PL model. For the same spectrum, Page et al. (2004) found $\Gamma = 2.34 \pm 0.04$ and a reflection parameter $R = 2.87 \pm 0.96$, which is consistent with our result, i.e., $R = 3.6^{+2.6}_{-1.6}$. Lanzuisi et al. (2016) have recently published the analysis of a deep (~100 ks) *NuSTAR* observation of J1250+2631 confirming the steep photon index and the presence of strong reflection in this source. These authors interpret the large R in terms of variability of the primary continuum, whereby the intense reflection component represents the light echo of a higher continuum level.

3.3. X-ray properties of WISSH quasars: absorption, fluxes, and luminosities

The left panel of Fig. 2 shows the distribution of the absorption column densities of X-ray detected WISSH quasars. Sources for which the PL model represents the best fit are included in the bin at $N_{\rm H} < 5 \times 10^{21}$ cm^{-2}. In case of $N_{\rm H}$ derived by HR analysis, we consider the values corresponding to the measured HR (i.e., the values in parentheses in Table 2, Col. 3). More than half of the sample (i.e., 60%) exhibits a $N_{\rm H}$ value < 10^{22} cm^{-2}, i.e., they are unobscured in X-rays. About 23% of the sample is moderately obscured with 10^{22} cm^{-2} ≤ $N_{\rm H}$ ≤ 10^{23} cm^{-2}. Accordingly, the bulk (~70%) of $N_{\rm H}$ result to be <5×10^{22} cm^{-2}, which agrees with the broad-line classification of WISSH quasars.

In the right panel of Fig. 2 we plot the $N_{\rm H}$ derived by spectral analysis versus the dust reddening values for X-WISSH quasars. The values of $A_{\rm V}$ were calculated from the color excess $E(B-V)$ through the relation $A_{\rm V} = 3.1 \times E(B-V)$. The color excesses were estimated by the SED fitting (Duras et al. 2017). The black square represents values of $N_{\rm H} = 5 \times 10^{21}$ cm^{-2} and $A_{\rm V} = 0$ found for eight sources. The blue solid line indicates the relation calculated by assuming a Galactic dust-to-gas standard value (Maiolino et al. 2001). It is evident that WISSH quasars have low $A_{\rm V}/N_{\rm H}$ ratios, which is apparently in contrast with the postulate of the unified model, which states that the dusty torus is the only responsible for the obscuration of both the X-ray and UV-optical nuclear radiation. Lower $A_{\rm V}/N_{\rm H}$ values compared to the Galactic value are usually explained according to a scenario in which our line of sight does not intercept the torus but a dust-free X-ray absorbing gas, which is likely located within the dust sublimation radius (i.e., in the broad-line region, BLR, Bianchi et al. 2012). As pointed out by Maiolino et al. (2001), another possible explanation may be related to a different dust composition in the surrounding region of AGN. Specifically, larger grains cause less extinction than the grains in the diffuse Galactic medium.

X-WISSH quasars show hard X-ray (i.e., 2–10 keV) fluxes ranging from ~7×10^{-15} up to few 10^{-13} erg cm^{-2} s^{-1}, with the bulk of these objects (more than 80%) exhibiting $10^{-14} < F_{2-10} < 10^{-13}$ erg cm^{-2} s^{-1}. Concerning the unabsorbed hard X-ray luminosities, the majority of sources have $10^{45} < L_{2-10} < 10^{46}$ erg s^{-1} (see Table 2).

Figure 3 shows the best-fit value of the photon index inferred from our spectra analysis as a function of the $\alpha_{\rm OX}$ spectral index. The $\alpha_{\rm OX}$ is defined as

$$\alpha_{\rm OX} = \frac{\log(L_{2\,\rm keV}/L_{2500\ \text{Å}})}{\log(\nu_{2\,\rm keV}/\nu_{2500\ \text{Å}})}, \quad (2)$$

i.e., it represents the slope of a power law defined by the rest-frame monochromatic luminosities at 2500 Å and 2 keV (Avni & Tananbaum 1982). For the calculation of the $\alpha_{\rm OX}$ for the WISSH quasars (see Table 2) we used the rest-frame 2500 Å monochromatic luminosities obtained by SED fitting (Duras et al. 2017). We find that the two sources with the steepest $\alpha_{\rm OX}$ also have the flattest X-ray continuum slope (i.e., X-ray faint compared to optical). However, the limited number of objects and the large uncertainties affecting some Γ values does not allow us to draw any firm conclusion on a possible trend.

Finally, our analysis of X-WISSH includes *Chandra* observations of six quasars previously analyzed by Just et al. (2007) (i.e., J0735+2659, J0900+4215, J1014+4300, J1106+6400, J1236+6554, and J1621-0042). The X-ray luminosities and spectral properties we derive for these objects are consistent with their results. Furthermore, our reanalysis of the ~37 ks *Chandra* observation of J1521+5202 confirms the results recently published by Luo et al. (2015), which also found a slightly flat ($\Gamma \sim 1.5$) continuum and an X-ray absorber with a $N_{\rm H} \sim 10^{23}$ cm^{-2}.

4. X-ray versus optical and MIR properties

4.1. X-ray-to-optical flux ratio (X/O)

The X-ray-to-optical flux ratio (X/O hereafter) is commonly used to provide a basic classification for X-ray sources without optical identification (Fiore et al. 2003; Brandt & Hasinger 2005). The bulk of AGN detected in the X-ray surveys exhibit

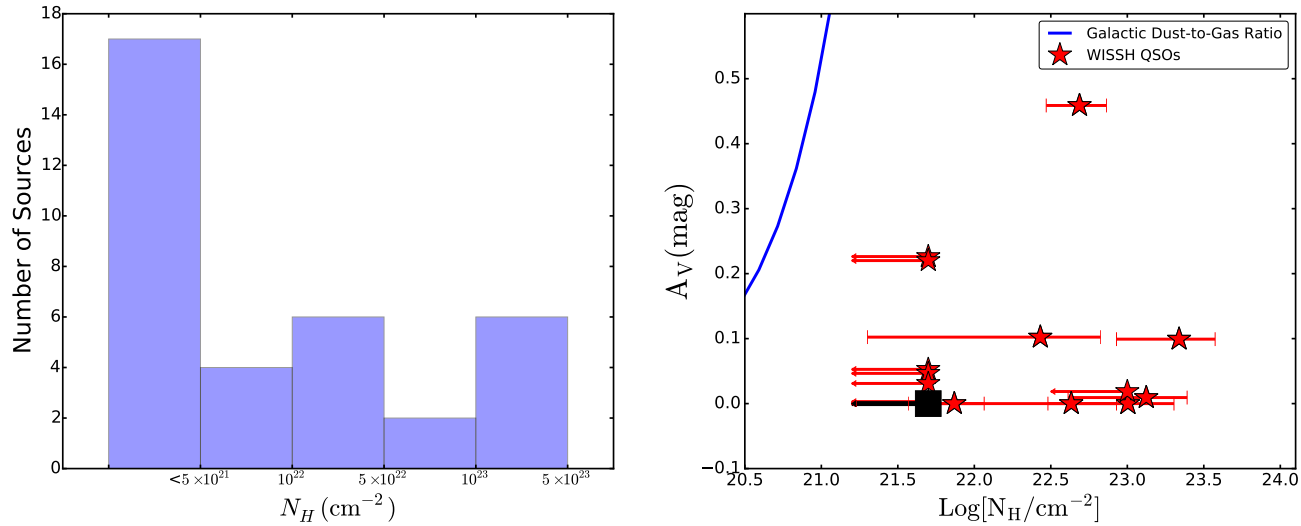

Fig. 2. *Left panel*: distribution of absorption column densities for the 35 X-ray detected quasars, derived by HR or spectral analysis. *Right panel*: A_V magnitudes vs. X-ray absorption column densities derived by spectral analysis. The black square represents values of $N_H = 5 \times 10^{21}$ cm^{-2} and $A_V = 0$ for 8 sources (see Table 2). The blue solid line represents the relation obtained by assuming a Galactic dust-to-gas ratio, i.e., $A_V = 10^{(\log N_H - 21.278)}$ mag (Maiolino et al. 2001).

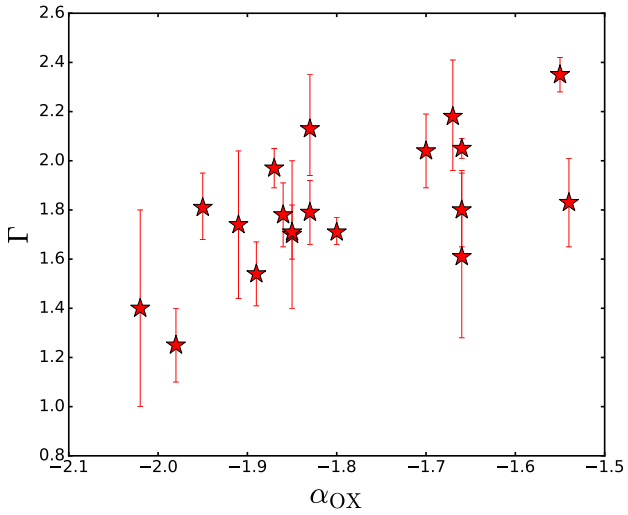

Fig. 3. Best-fit values of the photon index Γ from the spectral analysis as a function of the α_{OX} spectral index for X-WISSH quasars. The sources for which the Γ has been fixed to 1.8 in the spectral analysis are not included (e.g., Table 2).

$0.1 < X/O < 10$, while sources with larger and smaller X/O are typically associated with obscured AGN and normal and star-forming galaxies, respectively. In the calculation of the X/O ratio for the X-WISSH quasars we used hard X-ray fluxes and *i* magnitudes (following the COSMOS survey; see Civano et al. 2012), which are publicly available from the SDSS. The typical magnitudes of our objects range from 16 up to ∼18, with almost 50% of the sources showing $17 \lesssim i \lesssim 17.6$, as listed in Table 1. Given the redshift of X-WISSH quasars ($2 \lesssim z \lesssim 4$), the *i* band centered at ∼7600 Å approximately covers the range from ∼2500 Å to 1500 Å. Values of X/O for X-WISSH quasars are reported in Col. 7 of Table 2.

In the left panel of Fig. 4 the X/O for X-WISSH quasars is shown as a function of L_{2-10}. BAL quasars within our sample (see Table 1) are represented with green symbols and non-BAL WISSH with red symbols. Information about optical rest-frame spectral properties are also reported since 14 out of 41 X-WISSH sources, i.e., ∼35% of the sample, have available LBT-LUCI spectroscopy (Bischetti et al. 2017; Vietri et al., in prep.) and are represented with filled symbols. More specifically, stars indicate quasars with a broad and blueshifted [OIII] emission line (5 out of 41, ∼12%), while diamonds (8 out of 41, ∼20%) represent sources with broad CIV emission line strongly blueshifted (>2000 km s^{-1}) with respect to the Hβ emission line (indicative of powerful radiatively driven winds in the BLR), and very weak or absent [OIII] emission. Interestingly, there is a hint that quasars showing [OIII] outflows tend to populate the high X/O–high L_{2-10} region of the plane.

In the right panel of Fig. 4 we compare the X/O derived for the X-WISSH quasars (red stars), to those of other AGN samples, i.e., sources in the *Chandra* COSMOS (Civano et al. 2012) and 4Ms *Chandra* Deep Field South (CDFS) catalog (Xue et al. 2011). The subsample of CDFS sources used here has been obtained by matching the CDFS 4Ms catalog by Xue et al. (2011) with the GOODS-MUSIC optical multiband catalog (Vanzella et al. 2008). Only COSMOS and CDFS objects with $L_{2-10} > 3 \times 10^{42}$ erg s^{-1} were considered in order not to be contaminated by non-AGN sources. This sample of X-ray selected AGN consists of 1658 objects, out of which 296 are Type 1 AGN (blue triangles), 260 are Type 2 AGN (open circles), and the remaining sources (i.e., 1102) are unclassified AGN (black crosses). We also plot the X/O values for 23 optically selected quasars from the Palomar-Green (PG) Bright Quasar Survey of the complete sample by Laor et al. (1994). It is evident from Fig. 4 that WISSH quasars have very low X-ray-to-optical flux ratios ($X/O < 0.1$) compared to typical AGN values of $0.1 < X/O < 10$ measured for the COSMOS, CDFS, and PG sample. Nonetheless, WISSH quasars exhibit the largest hard X-ray luminosities, reaching extreme values of $L_{2-10} \approx 10^{46}$ erg s^{-1} and low levels of X-ray absorption.

Fiore et al. (2003) reported the existence of a correlation between X/O and X-ray luminosity for narrow-line AGN. This trend can be also observed in Fig. 4, where Type 2 AGN show increasing X/O values at increasing L_{2-10}, although with a large scatter. A possible explanation for this is the largely reduced optical-UV light from these obscured objects; this implies that

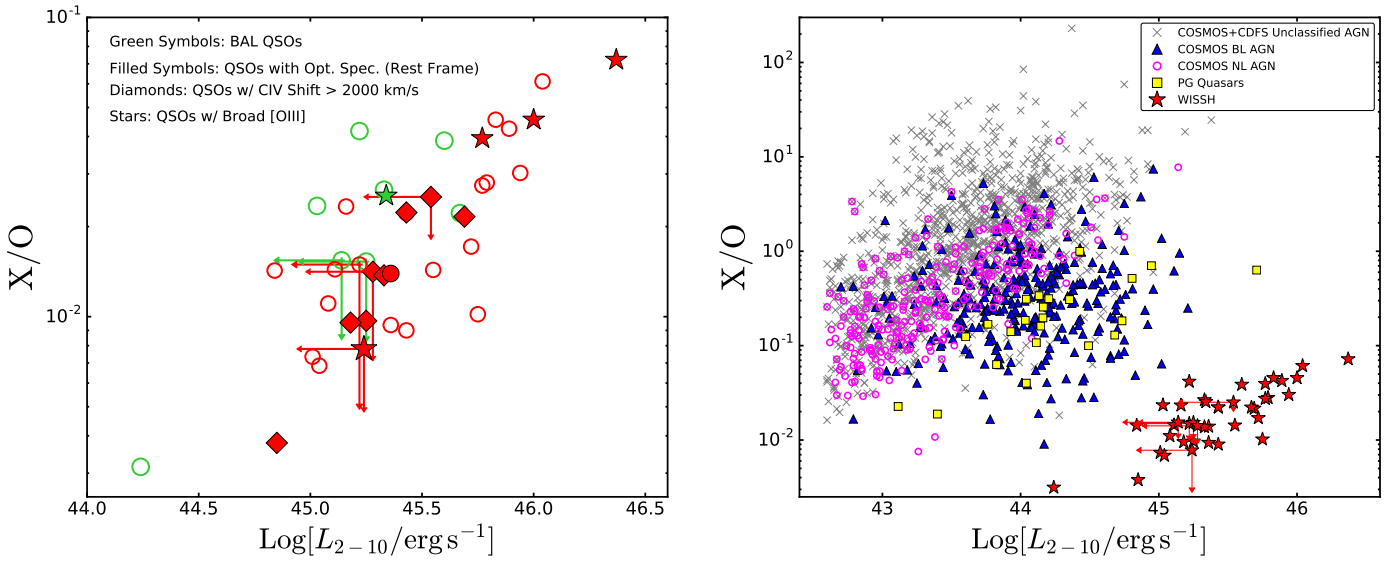

Fig. 4. Value of X/O as a function of unabsorbed 2–10 keV luminosity. *Left panel*: X-WISSH quasars are plotted; BAL WISSH quasars are represented with green symbols, while non-BAL WISSH are represented with red symbols. Filled symbols indicate objects that have an LBT-LUCI optical spectrum. Star and diamond symbols indicate the presence of broad [OIII] emission lines and CIV shifts >2000 km s^{-1}, respectively. *Right panel:* X-WISSH quasars (red stars) are compared to *Chandra* COSMOS, CDFS, and PG quasars. Blue triangles indicate the X-ray selected broad-line COSMOS AGN, while open circles indicate X-ray selected narrow-line COSMOS AGN. Unclassified X-ray selected AGN of both COSMOS and CDFS are represented with black crosses. Finally, yellow squares indicate PG quasars.

their X/O approximately represents the ratio between the AGN hard X-ray flux, which is less affected by the absorption than the optical-ultraviolet flux, and the host galaxy flux. Figure 4 suggests the presence of a correlation between the X/O and L_{2-10} for WISSH quasars. This is very unexpected as no correlation between X/O and hard X-ray luminosity has been reported for broad-line AGN so far. However, this trend can be explained in terms of a selection bias because of the limited range of i magnitude of WISSH quasars, with a median value of $i \sim 17.1$, as opposed to their X-ray luminosity, which ranges from a few 10^{44} up to values larger than 10^{46} erg s^{-1}.

4.2. X-ray-to-optical index (α_{OX} versus $L_{2500\ \text{Å}}$)

While the X/O ratio is calculated by observed quantities (i.e., fluxes), the α_{OX} is estimated by considering rest-frame, intrinsic properties, i.e., luminosities. In unobscured AGN, α_{OX} provides a basic indication of the relative strength between the emission produced in the accretion disk (at 2500 Å rest frame) and that emitted via Compton upscattering in the hot corona (at 2 keV rest-frame), by connecting two spectral regions encompassing the energy range where the bulk of the AGN radiative output is generated. The existence of an anticorrelation between α_{OX} and $L_{2500\ \text{Å}}$ is now well established (Vignali et al. 2003; Steffen et al. 2006; Lusso et al. 2010), indicating that the relative contribution of the X-ray emission to the total energy output decreases for increasing optical (and bolometric) luminosity.

Figure 5 shows the α_{OX} distribution for the X-WISSH quasars as a function of $L_{2500\ \text{Å}}$, calculated with the absorption-corrected X-ray luminosity. This demonstrates that WISSH quasars are in broad agreement with the α_{OX}–$L_{2500\ \text{Å}}$ anticorrelation, i.e., when compared with less luminous AGN, the most luminous quasars exhibit a weaker X-ray luminosity. The α_{OX} values derived for our hyper-luminous objects are plotted with those of other Type 1 AGN samples at lower L_{Bol}. Blue open triangles represent the broad-line AGN sample from the XMM-COSMOS survey by Lusso et al. (2010, L10 hereafter), while PG quasars are indicated with yellow squares as in Fig. 4. We have also included information on BAL objects, represented with green symbols. The WISSH symbols are as in Fig. 4. We also plot the linear relation found by L10 (dashed line), the relation by Just et al. (2007) (dash-dotted line), and the linear relation we derived by fitting the values of the XMM-COSMOS, PG, and X-WISSH samples together. The best-fit relation for $\alpha_{OX} - L_{2500\ \text{Å}}$, treating $L_{2500\ \text{Å}}$ as the independent variable results to be

$$\alpha_{OX} = (-0.172 \pm 0.006) \times \log(L_{2500\ \text{Å}}/\text{erg s}^{-1}\ \text{Hz}^{-1}) + (3.72 \pm 0.17), \quad (3)$$

where the errors on the slope and intercept indicate 1σ significance. The Spearman's rank test gives a rank coefficient of $\rho_s = -0.75$ and the probability of deviation from a random distribution is $d_s \sim 10^{-20}$, confirming a very robust anticorrelation between α_{OX} and $L_{2500\ \text{Å}}$.

Finally, in the inset of Fig. 5, open pentagons indicate absorption-corrected α_{OX} values for X-WISSH quasars, while gray open circles indicate α_{OX} values when X-ray absorption is not taken into account. The asterisks indicate α_{OX} for the six undetected sources, derived assuming the median value of the N_H measured in the X-WISSH sample, i.e., $N_H = 8 \times 10^{21}$ cm^{-2}. The error bars are calculated with $N_H = 0$ and $N_H = 4 \times 10^{23}$ cm^{-2}, i.e., the largest N_H of the sample. This plot highlights that once corrected for X-ray absorption, the steeper α_{OX} (typically associated with BAL quasars, marked in green) flatten to values broadly consistent with the L10 relation. A largely suppressed luminosity at 2 keV, and in turn a very steep $\alpha_{OX} < -3$ value, measured in our sources can be therefore ascribed to obscuration along our line of sight to the AGN.

4.3. X-ray to MIR luminosity relation

The WISSH quasars are among the most luminous AGN in the MIR, as they are selected to have $z > 1.5$ and WISE 22 μm flux density $S_\nu(22\ \mu\text{m}) > 3$ mJy (3σ). This allows us to explore and

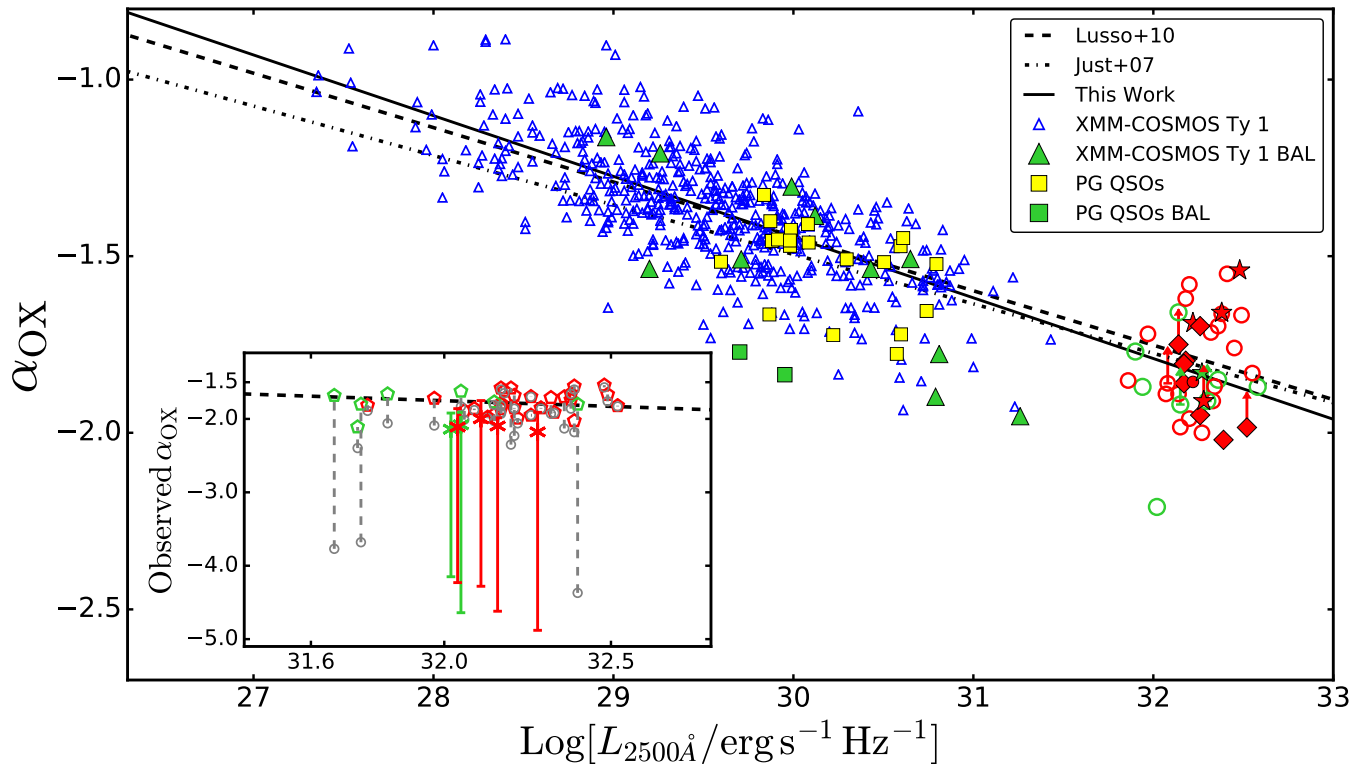

Fig. 5. Values of α_{OX} as a function of extinction-corrected 2500 Å monochromatic luminosities. Symbols for WISSH quasars as in Fig. 4. Blue triangles indicate the broad-line AGN sample from the *XMM-Newton*-COSMOS survey by Lusso et al. (2010); the yellow squares indicate PG quasars. Green symbols represent BAL AGN. The dashed line represents the relation found by Lusso et al. (2010), the dash-dotted line represents the Just et al. (2007) relation, and the black solid line indicates our linear fit. In the inset on the lower left corner of the figure, the open pentagons indicate absorption-corrected α_{OX} values; the gray open circles indicate α_{OX} values when X-ray absorption is not taken into account. The asterisks with error bars indicate α_{OX} values for the undetected X-WISSH sources, calculated with the N_H median value of the sample, i.e., $N_H = 8 \times 10^{21}$ cm^{-2}. The error bars were calculated using $N_H = 0$ and $N_H = 4 \times 10^{23}$ cm^{-2}, i.e., the maximum value of the sample.

extend the correlations involving the MIR luminosity up to the highest values. The X-ray and MIR emission of AGN are believed to be strongly linked, since the former is due to accretion onto the SMBH while the latter is interpreted in terms of reprocessed nuclear light from the surrounding absorbing material. A correlation between these two quantities based on the analysis of samples of local Seyfert galaxies and X-ray selected AGN has indeed been found (e.g., Lutz et al. 2004; Mateos et al. 2015 and references therein). Furthermore, Fiore et al. (2009) and Lanzuisi et al. (2009) discovered that quasars hosted in heavily dust obscured galaxies typically exhibit a lower L_X/L_{MIR} ratio than that reported for "standard AGN", suggesting a more complex scenario for the L_X–L_{MIR} relation in AGN.

As commonly adopted in recent works, we also used the 6 μm luminosity ($\lambda L_{6\,\mu m}$) as a proxy of the MIR luminosity, since emission due to AGN heated dust peaks around this wavelength. $\lambda L_{6\,\mu m}$ of WISSH quasars have been estimated by UV-to-MIR SED fitting (Duras et al. 2017) and span from $\sim 6 \times 10^{46}$ to $\sim 3 \times 10^{47}$ erg s^{-1}. Figure 6 shows L_{2-10} as a function of $\lambda L_{6\,\mu m}$ for the X-WISSH sources and a large compilation of AGN samples selected according to different criteria to mitigate any possible bias and obtain a better sampling of the L_{2-10}–$\lambda L_{6\,\mu m}$ plane. By including a total of 1749 AGN, we are able to explore the X–MIR luminosity relation in the ranges $42.5 \lesssim \log(L_{2-10}/\mathrm{erg\,s^{-1}}) \lesssim 46.5$ and $43.5 \lesssim \log(\lambda L_{6\,\mu m}/\mathrm{erg\,s^{-1}}) \lesssim 48$. More specifically, we include AGN from the *Chandra* COSMOS and CDFS surveys and the PG quasars (as in Fig. 4), and a sample of 24 MIR luminous quasars ($\lambda L_{6\,\mu m} \geq 6 \times 10^{44}$ erg s^{-1}) at redshifts $z \sim 1$–3, with X-ray luminosity derived by spectral analysis from Del Moro et al. (2016) (cyan pentagons). Finally, we also add the quantities for three hyper-luminous quasars (namely, ULASJ 1539+0557, ULASJ 2315+0143, and 2QZ0028-2830; indicated as violet asterisks), which show luminosities comparable to those measured for X-WISSH (see Appendix A). We also plot the L_{2-10}–$\lambda L_{6\,\mu m}$ relations derived by four previous works as follows: (i) the relation by Mateos et al. (2015) (black solid line), which has been obtained with a sample of >200 AGN from the Bright Ultra-Hard *XMM-Newton* Survey, including both broad- and narrow-line AGN with X-ray luminosities $10^{42} < L_{2-10} < 10^{46}$ erg s^{-1} and redshifts $0.05 < z < 2.8$; (ii) the relation reported in Lanzuisi et al. (2009) (black dashed line) with MIR-selected, dust-obscured, with MIR-to-optical flux ratio $F_{24\,\mu m}/F_R > 2000$, luminous quasars at $z \sim 1$–2 with $L_{2-10} \geq 10^{43}$ erg s^{-1}; (iii) the polynomial relation derived by Stern (2015) (black dotted curve) based on ~200 AGN with luminosities spanning from the local Seyfert regime to the hyper-luminous quasar regime, which accounts for a progressive decrease of $L_{2-10}/\lambda L_{6\,\mu m}$ by moving towards the highest luminosities; and (iv) the bilinear function by Chen et al. (2017) (black dash-dotted curve) which was recently derived by including more than ~2500 Type 1 AGN from four different X-ray surveys, i.e., Boötes, XMM-COSMOS, XRT-SDSS, and XXL-North, covering L_{2-10} in the range 10^{41}–10^{46} erg s^{-1} and $\lambda L_{6\,\mu m}$ up to 10^{47} erg s^{-1}.

As expected, X-WISSH quasars are located far below the Mateos et al. relation and most of these quasars are located even below the Lanzuisi et al. relation. Figure 6 points out the existence of a large scatter in the measurement of L_{2-10} at a

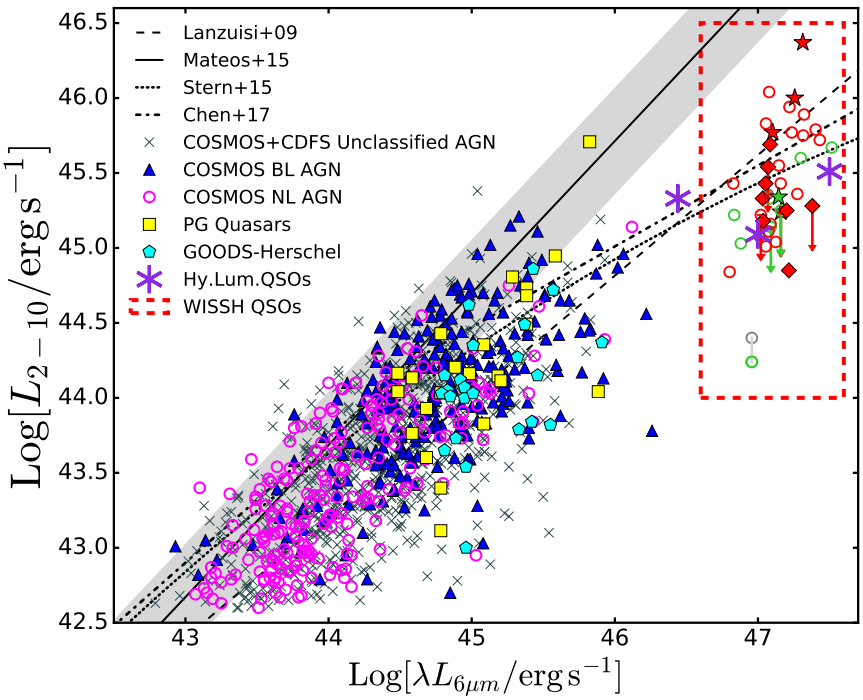

Fig. 6. Absorption-corrected 2–10 keV luminosity as a function of MIR luminosity at 6 μm (symbols as in Fig. 4). The cyan pentagons represent the MIR luminous quasars sample from the GOODS-*Herschel* fields presented by Del Moro et al. (2016). The violet asterisks indicate the hyper-luminous quasars ULAS J1539+0557, ULAS J2315+0143 and 2QZ0028-2830 (see Appendix A). The black solid, dashed, dotted, and dash-dotted lines represent the Mateos et al. (2015), Lanzuisi et al. (2009), Stern (2015), and Chen et al. (2017) relations, respectively. The gray shaded area indicates the intrinsic scatter about the Mateos relation. The red dashed line box indicates the locus of the WISSH quasars. We report two values for the hard X-ray luminosity of J0045+1438 (i.e., the object with the lowest X-ray luminosity in the X-WISSH sample) connected by a gray line. We calculated the L_{2-10} using the HR-based value of $N_{\rm H}$ (i.e., 4×10^{22} cm^{-2}, green open circle) and the upper error (i.e., $N_{\rm H} = 1.5 \times 10^{23}$ cm^{-2}, gray open circle), respectively.

given $\lambda L_{6\,\mu\rm m}$, once AGN selected with different criteria have been taken into account. This suggests that using a universal $L_{\rm X}$−$L_{\rm MIR}$ relation for evaluating the X-ray luminosity of a source can lead to a heavily over- or underestimated value. Still we reinforce previous results (e.g., Lanzuisi et al. 2009; Stern 2015; Chen et al. 2017) indicating that MIR luminous sources clearly offset from the $L_{\rm X}$−$L_{\rm MIR}$ relation derived for local Seyfert and X-ray-selected AGN. This suggests that in AGN at the highest MIR luminosities, the relative contribution from X-ray emission to the bolometric luminosity progressively decreases with respect to the MIR emission (see Sect. 6 for a detailed discussion). We also attempt to interpret the observed trend in the $L_{\rm X}$−$L_{\rm MIR}$ relation in terms of a luminosity-dependent covering factor ($C_{\rm f}$) of the torus. We assume $L_{\rm MIR} \propto C_{\rm f} \times L_{\rm UV}$ ($\approx L_{\rm Bol}$) and the $C_{\rm f}$ as a function of the luminosity at 5100 Å derived by Maiolino et al. (2007, see their Eq. (3)[5]) for a combined sample of high-z luminous quasars, local quasars, and Seyfert galaxies; $L_{5100\ \text{Å}}$ are estimated from $L_{\rm UV}$ via the bolometric corrections in Runnoe et al. (2012a). Consistently, we derive L_{2-10} from $L_{\rm UV}$ according to Eq. (6) in Lusso et al. (2010), assuming $L_{2-10} = 1.61 \times L_{2\,\rm keV}$ (i.e., adopting $\Gamma = 2$). However, the resulting $L_{\rm X}$−$L_{\rm MIR}$ is unable to reproduce the observed decrease in $L_{\rm X}/L_{\rm MIR}$ at high luminosities, but instead shows an opposite trend. This suggests that the observed weakness of the X-ray emission relative to the MIR emission in quasars cannot be interpreted to first order as due to a luminosity-dependent $C_{\rm f}$.

Alternatively, the observed $L_{\rm X}$−$L_{\rm MIR}$ relation could be caused by the selection bias due to the inclusion of both X-ray and MIR selected sources collected from different areas of the sky, i.e., from pencil-beam surveys to all-sky surveys, along with a redshift bias, according to which the most luminous AGN have been preferentially collected at high z.

Given its importance for shedding light on the properties of accretion, reprocessing of the nuclear light and geometry of the circumnuclear medium in AGN, the $L_{\rm X}/L_{\rm MIR}$ ratio certainly deserves further and deeper investigation in the future. For instance, it would be very interesting to populate the right upper corner of the L_{2-10}−$\lambda L_{6\,\mu\rm m}$ diagram, by selecting AGN at the highest X-ray luminosities. Indeed, the recent work by Chen et al. (2017) has shown that the heterogeneous flux limits of the different X-ray surveys contribute significantly to the difference in the $L_{\rm X}/L_{\rm MIR}$ ratio behavior between low- and high-luminosity AGN. The planned eROSITA All-Sky X-ray survey (Merloni et al. 2012) will be therefore crucial to pick up a large sample of X-ray selected hyper-luminous quasars and provide unprecedented constraints on the behavior of the $L_{\rm X}$−$L_{\rm MIR}$ relation at $L_{2-10} > 10^{45}$ erg s^{-1}.

5. X-ray bolometric corrections and Eddington ratios

Thanks to their spectacular luminosities, WISSH quasars offer the opportunity to investigate the X-ray bolometric correction (defined as $k_{\rm Bol,X} = L_{\rm Bol}/L_{2-10}$) up to the highest luminosity values (i.e., $L_{2-10} \gtrsim 10^{45}$ and $L_{\rm Bol} > 10^{47}$ erg s^{-1}). Bolometric luminosities for X-WISSH quasars have been estimated by SED fitting (Duras et al. 2017) and they span from $L_{\rm Bol} \sim 2 \times 10^{47}$ to $>10^{48}$ erg s^{-1}.

[5] Maiolino et al. (2007) assumed $C_{\rm f}$ equal to the fraction of obscured AGN.

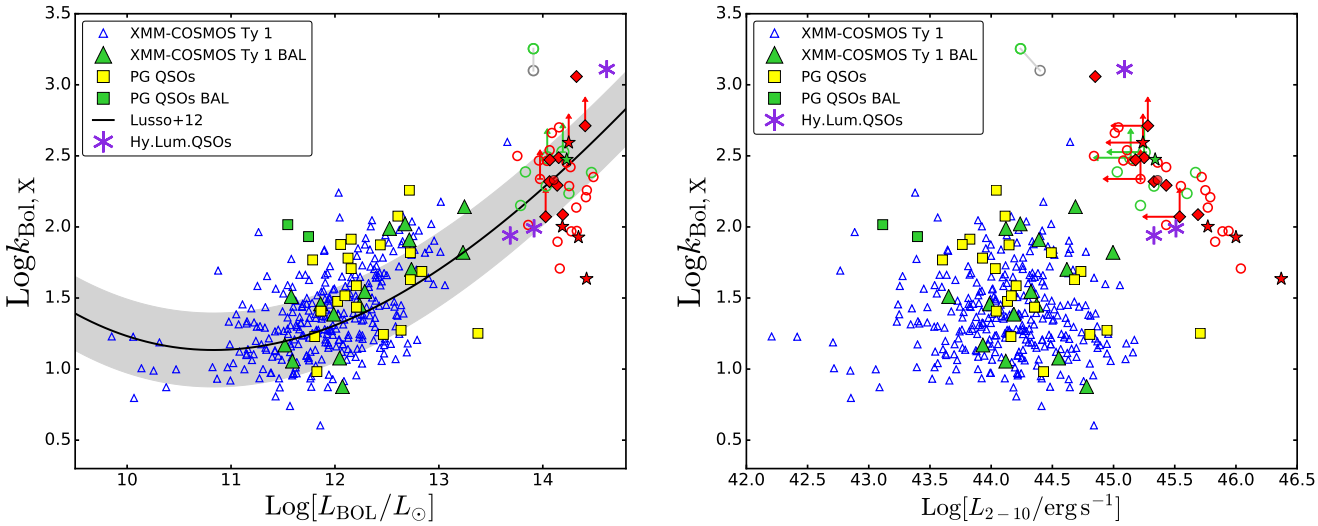

Fig. 7. Bolometric correction in the 2–10 keV band as a function of the bolometric luminosity (*left panel*) and as a function of the 2–10 keV luminosity (*right panel*). Symbols for the WISSH quasars follow those of Fig. 4. Blue triangles indicate the broad-line AGN sample from the *XMM-Newton*-COSMOS survey by Lusso et al. (2012). The yellow squares indicate PG quasars; green symbols represent BAL AGN. The violet asterisks indicate the hyper-luminous quasars ULASJ 1539+0557, ULASJ 2315+0143, and 2QZ0028-2830. The black solid curve in the *left panel* represents the relation found by Lusso et al. (2012) for Type 1 AGN; the gray shaded area indicates the 1σ dispersion on the relation. As in Fig. 6, we report two values for the hard X-ray luminosity of J0045+1438 (i.e., the object with the lowest X-ray luminosity in the X-WISSH sample), connected by a gray line. We calculated the L_{2-10} via the best-fit value of N_{H} (i.e., 4×10^{22} cm^{-2}, green open circle) and the upper error (i.e., N_{H} = 1.5×10^{23} cm^{-2}, gray open circle), respectively.

The left panel of Fig. 7 shows the $k_{\mathrm{Bol,X}}$ for the X-WISSH quasars as a function of L_{Bol}, while in the right panel $k_{\mathrm{Bol,X}}$ is plotted versus the 2–10 keV luminosity. Our sources (symbols as in Fig. 4) are compared to Type 1 AGN from the *XMM-Newton*-COSMOS survey (presented in Lusso et al. 2012, L12 hereafter, indicated as open triangles), PG quasars (yellow squares), and the hyper-luminous quasars ULASJ 1539+0557, ULASJ 2315+0143, and 2QZ0028-2830, which are represented with violet asterisks (see Appendix A). As in the previous figures, BAL quasars are indicated by green symbols. The black solid line represents the $k_{\mathrm{Bol,X}}$−L_{Bol} relation obtained by L12 for Type 1 objects in COSMOS. This curve also provides a good description for our hyper-luminous quasars (the scatter around the L12 relation is σ = 0.82 dex). Combining all the objects from these samples, the Spearman's rank correlation coefficient is ρ_{s} = 0.7 (and $d_{\mathrm{s}} < 10^{-20}$), indicating a strong correlation between $k_{\mathrm{Bol,X}}$ and L_{Bol}. The ratio of the X-ray luminosity over the bolometric luminosity provides the relative contribution of the corona and accretion disk to the total radiation output from the AGN. Therefore, the positive trend observed between $k_{\mathrm{Bol,X}}$ and L_{Bol} lends support to the scenario whereby the corona radiative power becomes progressively weaker with respect to the optical-UV disk emission at increasing bolometric luminosities. The right panel of Fig. 7 reinforces our conclusions on the extreme nature of WISSH quasars, which exhibit both exceptional X-ray luminosities and large bolometric corrections.

The multiband coverage of WISSH allows us to derive the SMBH mass (M_{BH}) for each quasar. Accordingly, we are able to study the behavior of $k_{\mathrm{Bol,X}}$ as a function of M_{BH} and Eddington ratio (λ_{EDD} = $L_{\mathrm{Bol}}/L_{\mathrm{EDD}}$). The SMBH mass for 14 out of 41 objects (∼35% of X-WISSH) are estimated from Hβ lines (Bischetti et al. 2017; Vietri et al., in prep.), while the remaining masses are calculated from CIV lines (Weedman et al. 2012). In the left panel of Fig. 8 we present the hard X-ray bolometric correction versus λ_{EDD}, while in the right panel $k_{\mathrm{Bol,X}}$ is shown as a function of the M_{BH}. Filled (open) stars represent WISSH quasars with Hβ (CIV)-based SMBH masses. The M_{BH} for COSMOS and PG quasars are computed using the width of the Hβ (or Mg II) emission line. Several authors claimed for a positive trend between $k_{\mathrm{Bol,X}}$ and λ_{EDD} (Vasudevan & Fabian 2007; Lusso et al. 2012), even if affected by large scatter. For the sources considered here, the total scatter with respect to the L12 relation is σ = 0.43 dex with a larger scatter observed at the highest values of $k_{\mathrm{Bol,X}}$ and λ_{EDD}. The Spearman's rank test gives a rank coefficient of ρ_{s} = 0.56, and the probability of deviation from a random distribution is $d_{\mathrm{s}} \sim 10^{-21}$, confirming a likely and robust correlation between the two quantities. Additionally, by fitting M_{BH} vs. $k_{\mathrm{Bol,X}}$, we found the following linear relation (see right panel of Fig. 8):

$$\log k_{\mathrm{Bol,X}} = (0.377 \pm 0.032) \times \log(M_{\mathrm{BH}}/M_{\odot}) - (1.67 \pm 0.28), \quad (4)$$

with a large scatter ($\sigma \simeq 0.4$ dex) and ρ_{s} = 0.4. Furthermore, the probability value is very low ($d_{\mathrm{s}} < 10^{-10}$). These values mean that the existence of a correlation between M_{BH} and $k_{\mathrm{Bol,X}}$ is significantly likely. The inclusion of WISSH quasars suggests that the largest values of $k_{\mathrm{Bol,X}}$ may be observed in objects at the massive end of the M_{BH} distribution.

The WISSH survey offers the opportunity of sampling extreme values of L_{Bol}, $k_{\mathrm{Bol,X}}$, M_{BH} and λ_{EDD} poorly sampled so far, i.e., $\gtrsim 10^{14}$ $L_{\odot}$, 10^{2}, 10^{10} $M_{\odot}$ and 0.5, respectively, as highlighted by Fig. 9, which shows the distribution of λ_{EDD} as a function of the SMBH mass for the AGN samples considered in Fig. 8.

A clear difference in the distribution of the M_{BH} is evident when comparing sources from X-WISSH to those from COSMOS and PG survey, which can be considered as representative of the most studied class of broad-line AGN in X-rays. We performed a Kolmogorov-Smirnov (KS) test to understand if they are consistent with having been sampled from the same parent distribution and we derived a p-value $<10^{-9}$ for both comparisons. Accordingly, WISSH sources truly represent an extreme class of AGN showing a M_{BH} distribution centered around 10^{10} $M_{\odot}$. When comparing $\log \lambda_{\mathrm{EDD}}$ of X-WISSH to COSMOS,

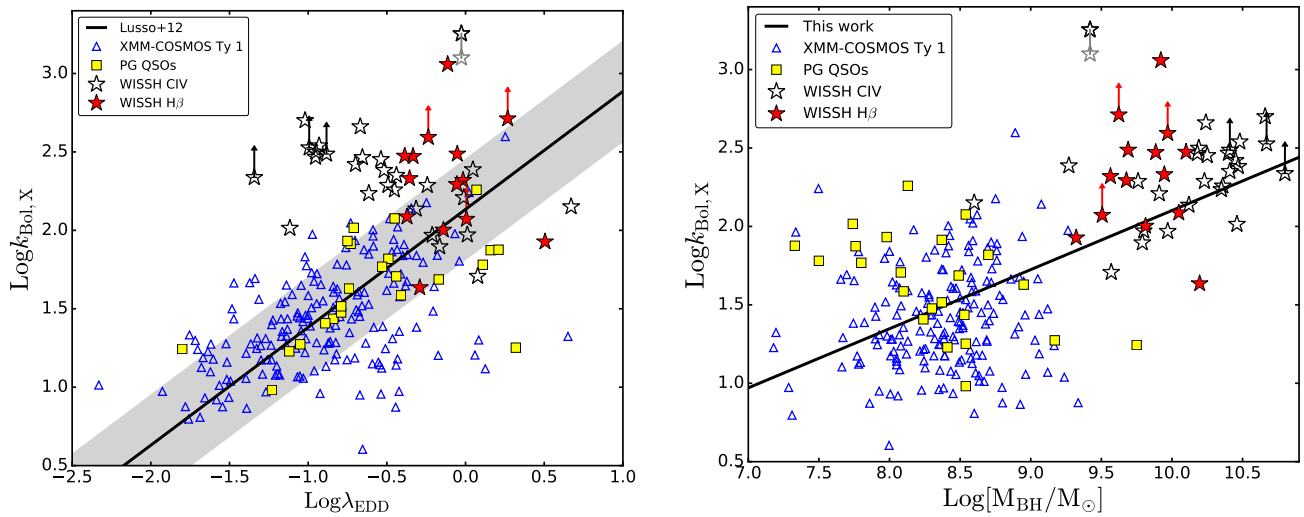

Fig. 8. Bolometric correction in the 2–10 keV band as a function of the Eddington ratio λ_{EDD} (*left panel*) and as a function of the black hole mass (*right panel*). The open stars represent WISSH quasars with CIV-based SMBH masses (Weedman et al. 2012); red filled stars represent Hβ-based SMBH masses (Bischetti et al. 2017, Vietri et al., in prep.). The blue empty triangles indicate the broad-line AGN sample from the *XMM-Newton*-COSMOS survey by Lusso et al. (2012). The yellow squares indicate PG quasars. The black solid line in the *left panel* represents the relation found by Lusso et al. 2012 for Type 1 AGN, while the gray shaded area indicates the 1σ dispersion on the relation. The black solid line in *the right panel* indicates the linear fit found in this work. As in Fig. 6, we report two values for the hard X-ray luminosity of J0045+1438, connected by a gray line. We calculated the L_{2-10} with the best-fit value of N_H (i.e., 4×10^{22} cm^{-2}, black open star) and the upper error (i.e., $N_H = 1.5\times10^{23}$ cm^{-2}, gray open star), respectively.

the p-value (i.e., the probability that they belong to the same parent distribution) is $\sim10^{-6}$, while this probability increases to $\sim$10% if the λ_{EDD} of X-WISSH and PG quasars are considered. However, the Hβ-based SMBH mass derived for randomly selected WISSH quasars with optical rest-frame spectroscopy seems to be typically smaller than those estimated from the CIV emission line. Coatman et al. (2017) reported a similar trend by comparing Hα-based with CIV-based M_{BH}, finding that CIV-based M_{BH} can be overestimated by up to a factor of $\sim$5, especially in case of highly blueshifted ($v_b > 1200$ km s^{-1}) CIV emission lines. The latter are detected in the majority of WISSH quasars (see Sect. 6; Vietri et al., in prep.), suggesting that the real distribution of the λ_{EDD} of WISSH quasars may be centered at much larger values. If we restrict the comparison to objects with more reliable Hβ-based masses, the probability that they belong to the same parent distribution decreases to 0.04%, which indicates that these two distributions are indeed different, thus confirming the extreme nature of WISSH sources.

Previous works focusing on the relation between the photon index Γ and M_{BH} found different behaviors. Specifically, Kelly et al. (2008) reported a strong monotonic decreasing trend for Hβ-based M_{BH} of low-z AGN, while Jin et al. (2012a) claimed the existence of two regimes, i.e., one decreasing up to $\log(M_{BH}/M_{\odot}) = 8$ and another slightly increasing at larger masses. In order to further investigate this relation, we extended the range of M_{BH} considered by Jin et al. (2012a) both at $\lesssim10^6$ and $\gtrsim10^9$ by including the Miniutti et al. (2009b) and Ludlam et al. (2015) samples of intermediate mass SMBHs and the WISSH quasars, respectively. Figure 10 shows the photon index Γ as a function of M_{BH} for these samples. We tried to be as unbiased as possible by the soft excess contamination. Indeed, we considered the slope of the primary hard X-ray power law derived by a fit with an additional spectral component to account for soft excess (i.e., Table 3 in Miniutti et al. 2009b; Ludlam et al. 2015) or those derived from a fit limited to the 2–10 keV band (Table 3 in Jin et al. 2012b). In case of high-M_{BH} objects, which in this case are all at high z[6], we adopted the photon index resulting from a power-law fit since the soft excess is outside the observed band. According to Fig. 10, a slightly decreasing trend with M_{BH}, possibly flattening at large values is visible. We have therefore fitted the data with both a (i) linear (χ^2/d.o.f. = 341/93) and a (ii) broken power-law (χ^2/d.o.f. = 304/91) relation finding the following best-fit parametrizations:

$$\text{(i)} \quad \Gamma = (-0.08 \pm 0.02)\log(M_{BH}/M_{\odot}) + (2.61 \pm 0.15) \tag{5}$$

$$\text{(ii)} \quad \Gamma = (-0.19 \pm 0.04)\log(M_{BH}/M_{\odot}) + (3.38 \pm 0.28) \tag{6}$$

for $\log(M_{BH}/M_{\odot}) \leq (8.01 \pm 0.48)$;

$$\Gamma = (0.006 \pm 0.045)\log(M_{BH}/M_{\odot}) + (1.79 \pm 0.28) \tag{7}$$

for $\log(M_{BH}/M_{\odot}) > (8.01 \pm 0.48)$. It can be seen that our broken power-law relation implies flatter Γ than that derived by Jin et al. (2012a) over the entire 10^5–10^{10} masses. This is likely due to the increased statistics at both extremes of M_{BH} range, which led to a better sampling of the overall Γ distribution. Unlike Jin et al. (2012a), we left the break in M_{BH} free to vary. We find, however, that our measured break is consistent with that assumed by Jin et al. (2012a). The much steeper relation reported by Kelly et al. (2008) can be explained in terms of the presence of an unfitted soft excess component in their power-law fit to the 0.3–7 keV spectra of low-z AGN. Our results suggest that the power-law slope depends weakly on M_{BH}. The modest increase measured at low masses might be ascribed to an enhancement of the emission from the accretion disk leading to a stronger X-ray corona cooling, in case of highly-accreting sources. This effect is more noticeable in low-z, low-M_{BH} sources (such as narrow emission line Seyfert galaxies; e.g., Kuraszkiewicz et al. 2000) by a stronger soft excess that manifests itself at progressively

[6] In addition to WISSH quasars with Γ derived via X-ray spectroscopy, we considered the five quasars at $z \gtrsim 1.5$ listed in Table 2 in Kelly et al. (2008) and the five quasars listed in Table 2 in Shemmer et al. (2008).

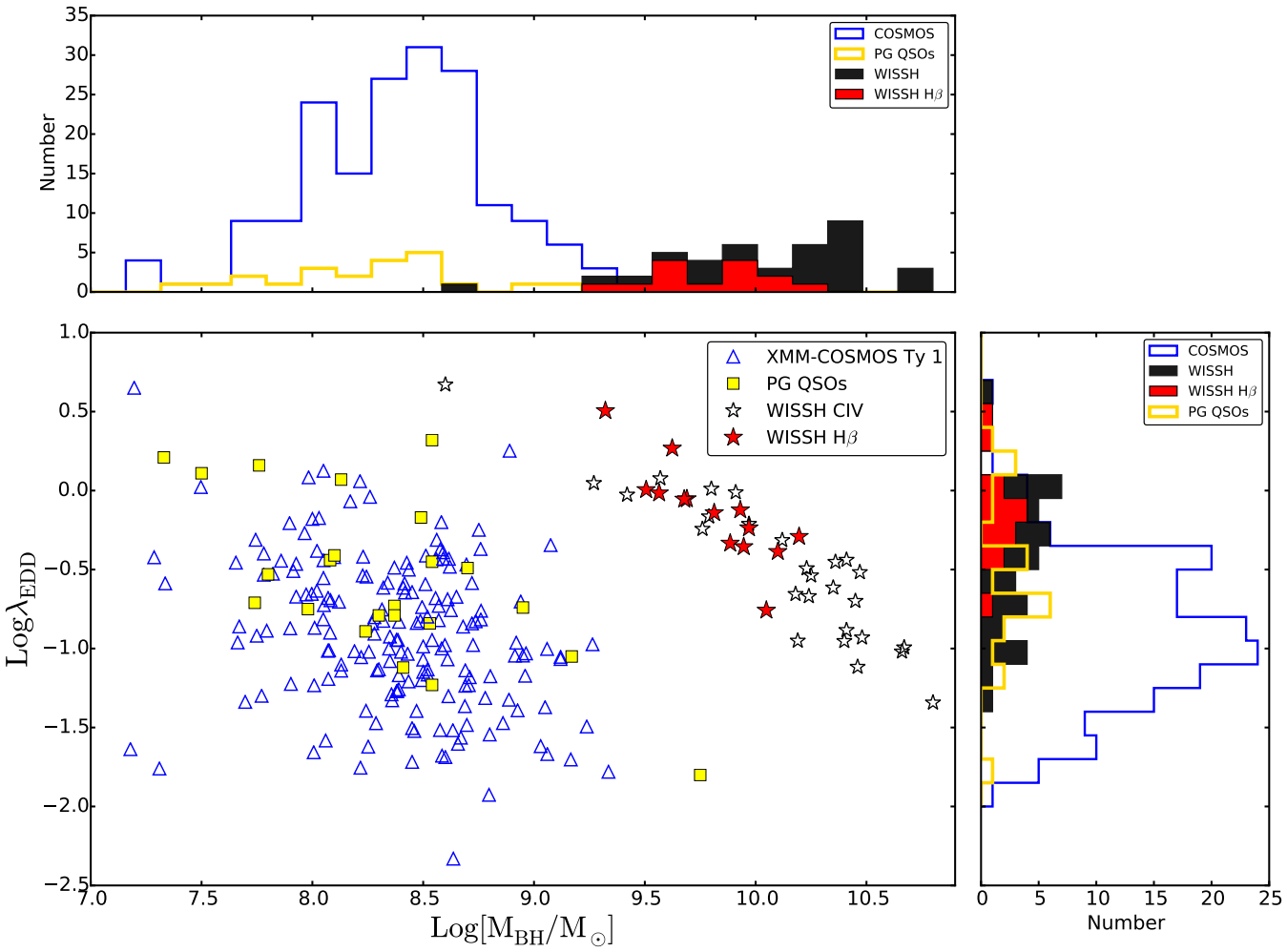

Fig. 9. Eddington ratios as a function of black hole masses. The distribution of the masses is indicated in the *upper panel*, while the distribution of Eddington ratios is shown on the *right* (Symbols as in Fig. 8).

harder energies. However, in order to obtain more comprehensive and less biased view of the Γ–M_{BH} relation, two major improvements are necessary at least: first, a significant increase of studied AGN with $M_{BH} \ll 10^7\ M_{\odot}$ to overcome the observed large scatter in Γ, and second, a homogeneous spectral analysis with an accurate modeling of the soft excess component of X-ray data in the widest possible energy range (i.e., by combining *XMM-Newton* and *Chandra* with simultaneous *NuSTAR* observations).

Figure 11 shows Γ as a function of $\log \lambda_{EDD}$ for the same sources of Fig. 10. Shemmer et al. (2008) and Brightman et al. (2013) reported the existence of a correlation between these two quantities (shown in Fig. 11 as a blue solid and dashed line, respectively). The former is based on 10 highly luminous radio-quiet AGN at $z = 1.3$–3.2 plus 25 less luminous PG quasars at $z < 0.5$, while the latter was obtained by including 69 X-ray selected, broad-line AGN up to $z \sim 2$ in COSMOS and Extended CDFS, with $10^{42.5} < L_{2-10} < 10^{45.5}$ erg s^{-1}. If, on the one hand, the data appear to be broadly consistent with the reported correlations, on the other hand, a large scatter is evident, especially for $-1 \leq \log \lambda_{EDD} \leq 0$. Furthermore, as expected, most of the steepest Γ are those from low-M_{BH} sources and these may both drive the correlation at high λ_{EDD} and contribute to the large scatter. Accordingly, before drawing a firm conclusion about the existence of a strong Γ–$\log \lambda_{EDD}$ correlation, the same improvements required for the Γ–M_{BH} should be taken in to account.

6. Conclusions and future work

6.1. Relative X-ray weakness of hyper-luminous quasars compared to less luminous AGN

We have investigated the X-ray properties of 41 sources from the sample of WISSH quasars, which includes among the most luminous AGN known. These sources exhibit $L_{2-10} \approx 10^{45-46}$ erg s^{-1}, i.e., well above the typical X-ray luminosity range of AGN extensively investigated in previous spectroscopic studies. Furthermore, the MIR selection enables us to extend and complete the study of the nuclear properties of hyper-luminous quasars, which have been mainly based on X-ray and/or optically selected AGN samples so far. As expected from their optical classification of broad-line objects, we found that most of these sources show a low level of X-ray absorption along the line of sight to the nucleus with a fraction of ~80% exhibiting intrinsic obscuration $N_H \leq 5 \times 10^{22}$ cm^{-2}. We found that WISSH quasars allow us to sample different ranges of the parameters space with respect to the bulk of the AGN population at lower luminosities when their X-ray output is compared to emission properties in other bands. The X/O colors derived for WISSH quasars are very low, i.e., $0.01 < X/O < 0.1$, and cannot be ascribed to an obscured X-ray emission, since, as expected from their optical classification of broad-line objects, we found that most of them show a low level of X-ray absorption along the line of sight to the nucleus (see Sect. 3.3). The largest X/O values observed for

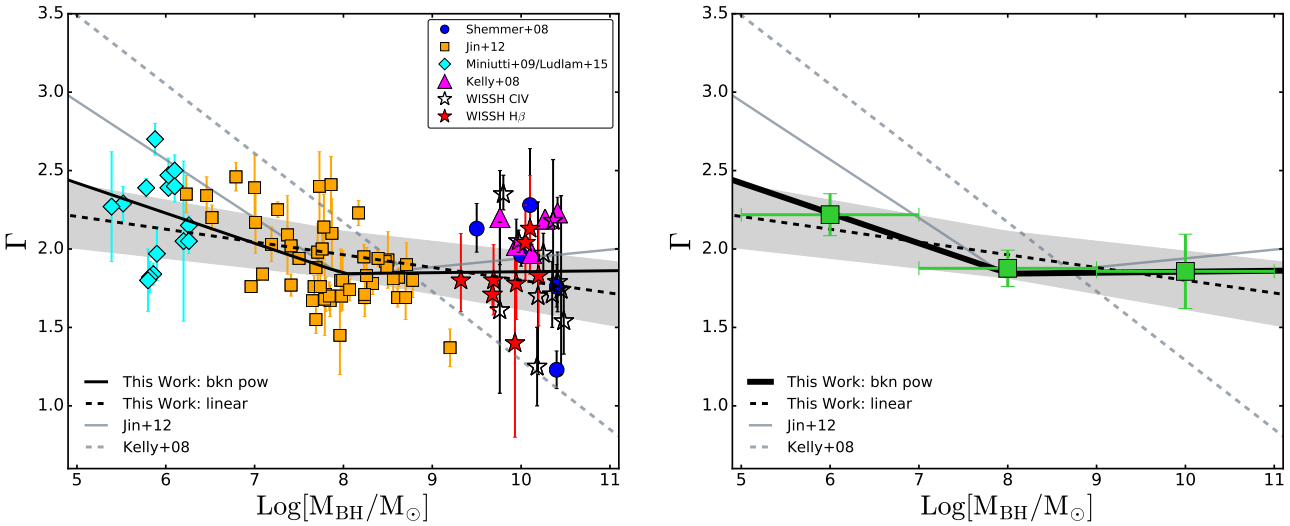

Fig. 10. *Left panel*: X-ray photon index as a function of $M_{\rm BH}$ for the X-WISSH quasars with X-ray spectroscopy (filled stars indicate objects with a Hβ-based SMBH mass; Bischetti et al. 2017; Vietri et al., in prep.) and while open stars indicate sources with a CIV-based SMBH mass (Weedman et al. 2012). We also report data for other samples as follows: the cyan diamonds indicate intermediate $M_{\rm BH}$ AGN by Miniutti et al. (2009b) and Ludlam et al. (2015); the orange squares denote the AGN from Jin et al. (2012a); the magenta triangles and blue circles represent high-z quasars from Kelly et al. (2008) and Shemmer et al. (2008), respectively. The black dashed and solid lines represent the linear and broken power-law relations found in this work; the gray shaded area indicates the combined uncertainties in slope and normalization. The gray dashed line and the solid line indicate the linear and broken power law found by Jin et al. (2012a) and Kelly et al. (2008), respectively. Errors on Γ are consistently reported at 90% c.l. for all the sources. *Right panel*: binned Γ over the following $\log(M_{\rm BH}/M_{\odot})$ ranges: 5–7, 7–9, and 9–11.

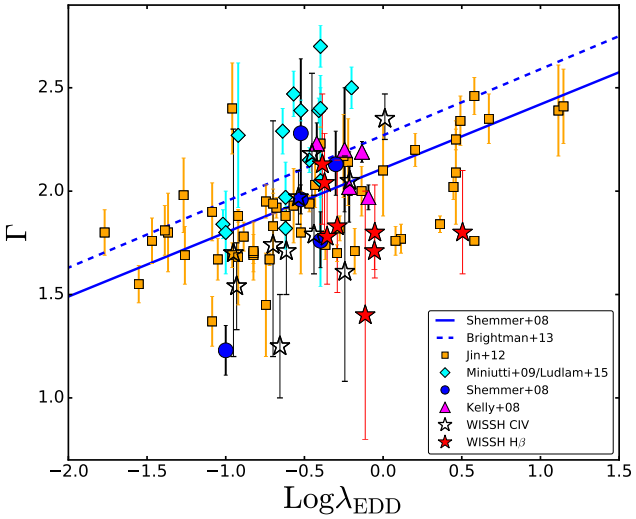

Fig. 11. X-ray photon index as a function of $\lambda_{\rm EDD}$ for the X-WISSH quasars with X-ray spectroscopy. Symbol as in Fig. 10. The blue solid line represents the relation found by Shemmer et al. (2008); the blue dashed line represents the relation by Brightman et al. (2013). Errors on Γ are consistently reported at 90% c.l. for all the sources.

less luminous sources in the CDFS and COSMOS survey ($0.1 <$ X/O < 10) can be partly explained by the X-ray selection. However, our results point out that luminous AGN can even reach X/O values as low as those so far reported for star-forming and quiescent galaxies (e.g., Barger et al. 2003). We also found that WISSH quasars follow the well-known $\alpha_{\rm OX}$–$L_{2500\ \text{Å}}$ anticorrelation (Vignali et al. 2003) by populating the bright end of the distribution with the steepest $\alpha_{\rm OX}$ (see Eq. (3) and Fig. 5). The combination of variability and non-simultaneity of UV and X-ray observations contributes to the observed large scatter in this relation, however it is not the main cause of dispersion as results based on simultaneous data clearly indicate (see Vagnetti et al. 2010). Steep $\alpha_{\rm OX}$ and, therefore, very low X/O clearly imply that, with respect to less luminous AGN, the X-ray emission of hyper-luminous quasars is relatively weaker as compared to the optical-UV emission. The results of our X-ray analysis therefore lend support to previous works that reported different SED for quasars with different luminosity. Krawczyk et al. (2013) analyzed the SEDs of 119 652 broad-line quasars detected in the SDSS with $0.064 < z < 5.46$ and found that the mean SED of high-luminosity sources, relative to the SED of low-luminosity sources, is characterized by a softer (i.e., redder) far-UV spectral slope, a bluer optical continuum, and a stronger hot dust emission peaking at 2–4 μm. Remarkably, the formation of radiation line driven winds from the accretion disk are favored in AGN with strong UV luminosity relative to the X-ray luminosity (i.e., X-ray weak). The efficiency of the line driving mechanism in accelerating the wind is indeed largely enhanced by the abundance of UV photons, while the soft UV-to-X-ray ionizing continuum avoids the overionization of the gas in the disk atmosphere (Leighly 2004; Proga 2003, 2007, and references therein).

This scenario is particularly relevant for high-ionization lines that originate closer to the primary continuum source than low-ionization lines. It also provides an explanation for the larger blueshifts ($v_{\rm b}$) of the CIV with respect to low-ionization emission lines such as MgII and Hβ found at higher luminosities in the wind-dominated quasar population (e.g., Richards et al. 2011; Marziani et al. 2016), and the observed anticorrelation between $v_{\rm b}$ and the EW of the CIV emission line (Korista et al. 1998; Krawczyk et al. 2013). This SED-based scenario for wind-dominated quasars rules out orientation as a major cause of these blueshifts. Such accretion disk winds have been also revealed in the majority of WISSH quasars with available rest-frame optical spectroscopy, showing $v_{\rm b}$ up to $\sim$7000 km s^{-1} (Vietri et al., in prep.). Figure 12 shows the $N_{\rm H}$ derived by our spectral X-ray analysis plotted versus $v_{\rm b}$. Gallagher et al. (2005) claimed that large $v_{\rm b}$ (>1100 km s^{-1}) quasars exhibit X-ray absorption

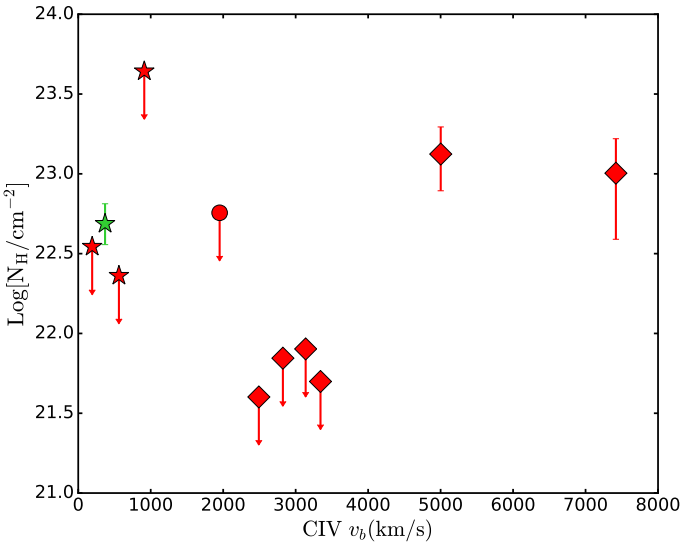

Fig. 12. N_H derived by spectral or HR analysis for the detected X-WISSH quasars as a function of CIV blueshift (v_b). Symbols as in Fig. 4.

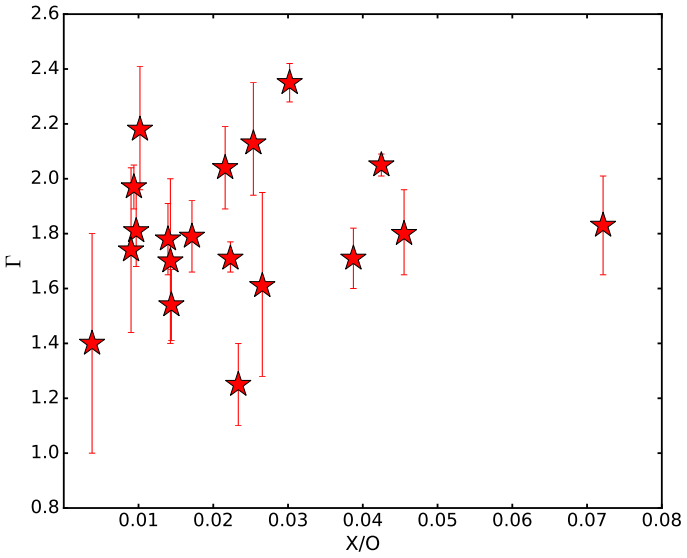

Fig. 13. X-ray photon index as a function of X/O for the X-WISSH quasars with X-ray spectroscopy.

at levels of $N_H > 10^{22}$ cm^{-2}, as expected in case of quasars observed at larger inclination angles, i.e., with a line of sight close to the accretion disk plane. However, we find that most of WISSH quasars with such large v_b values have $N_H \lesssim 10^{22}$ cm^{-2}, which is at odds with their claim that the detection of large blueshifts is due to an orientation effect.

Furthermore, a softer ionizing continuum scenario at larger luminosity explains the detection of CIV, NV, and SiIV BALs in quasars, and two anticorrelations reported by Brandt et al. (2000) and Laor & Brandt (2002) between α_{OX} and the EW of the CIV absorption line and between luminosity and maximum outflow velocity of absorption, respectively.

Remarkably, Proga (2005) suggests that highly accreting AGN can launch an UV radiation-driven accretion-disk wind because it is effective in weakening and destroying the X-ray corona and, therefore, quenching the X-ray emission. This explanation is very intriguing as it predicts different properties for the X-ray corona in powerful AGN that are linked to the simultaneous presence of nuclear outflows. In this sense, the extreme X-ray weakness of WISSH quasars exhibiting strongly blueshifted CIV emission lines (see Figs. 4 and 7) lends support to this scenario, although it is too early to draw robust conclusions owing to the small number of sources. Hyper-luminous quasars thus represent the ideal laboratory to study the coronal-quenching scenario and the link between the AGN energy output and wind acceleration, since they satisfy the ideal conditions to develop powerful radiation driven disk winds as found by Proga (2007), i.e., extreme L_{Bol} and very large M_{BH}.

Alternative explanations for the intrinsic X-ray weakness relative to UV in AGN have been proposed. Specifically, the X-ray under-luminosity could be due to a strong light bending effect that suppresses the X-ray continuum and produces a reflection-dominated X-ray spectrum (Schartel et al. 2010; Miniutti et al. 2009a); or, this under-luminosity could be a consequence of photon-trapping and advection into the SMBH of X-ray photons in case of high accretion rate regimes (e.g., Leighly et al. 2007). Furthermore, radiation magneto-hydrodynamic simulations presented by Jiang et al. (2014) suggest that, assuming a scenario in which the X-ray corona heated via dissipation of turbulence driven by magneto-rotational instability, X-ray weakness can occur when most of the energy liberated by accretion is dissipated in the disk due to a large surface density (and possibly associated with a very large accretion rate and luminosity). It might also be argued that the weakness observed in the 2–10 keV flux of our hyper-luminous quasars could partly be due to a Γ flatter than the canonical range of ∼1.8–2, which implies that the bulk of the X-ray radiation is emitted at energies larger than 10 keV. In this case, we should expect that sources with the flattest Γ would show the lowest X/O, offering a possible explanation for the X-ray weakness in terms of a flatness of the spectral index. However, Fig. 13 does not support this scenario and the Spearman's rank test results in a probability of deviation from a random distribution of $d_s = 0.34$, indicating no significant correlation between X/O and Γ.

The observed displacement of luminous quasars from the $L_X - L_{MIR}$ relation inferred for low-luminosity AGN (see Sect. 4.3 and Fig. 6) can be accounted for by the relative X-ray weakness progressively emerging in objects at the bright end of the AGN luminosity function compared to the slowly decreasing bolometric correction in the MIR (Treister et al. 2008; Runnoe et al. 2012b). In addition to this effect, the low L_{2-10}-to-$\lambda L_{6\,\mu m}$ ratios derived for WISSH quasars can be also caused by the strong AGN-heated, hot dust emission typically observed in the mean SED of hyper-luminous quasars (Krawczyk et al. 2013). This leads to a luminosity-dependent $L_X - L_{MIR}$ relation, although the observed large scatter in the L_{2-10}–$\lambda L_{6\,\mu m}$ plane severely challenges the idea of the existence of an universal relation. Furthermore, an explanation in terms of a luminosity-dependent C_f is not able to reproduce the observed trend at large L_{MIR}.

The presence of a relatively weaker X-ray corona in hyper-luminous quasars compared to typical AGN is further supported by the increasing $k_{Bol,X}$ with L_{Bol} (see Fig. 7). The WISSH quasars typically exhibit $k_{Bol,X} \gtrsim 100$, which demonstrates a significantly reduced contribution of the X-ray emission to the radiation output produced by the accretion disk-corona system in the powerful quasar regime. A deeper investigation based on a large sample of luminous quasars with well-determined X-ray spectral

information and M_{BH} is also crucial to establish the possible dependence of $k_{Bol,X}$ on λ_{EDD} and M_{BH}, and, if a strong correlation is observed, to understand which is the dominant parameter among L_{Bol}, λ_{EDD}, and M_{BH}. This will also improve our understanding of the relation between Γ and M_{BH}, for which we derived a double power-law behavior flatter than previously found by other works (see Sect. 5). The WISSH quasar sample offers a unique data set to perform such a study as shown in Fig. 9.

6.2. Future perspective with Athena

We discuss here the possible development in the study of the X-ray properties of WISSH quasars in the light of the ESA next X-ray observatory *Athena* (Nandra et al. 2013). The marked improvement in sensitivity and spectral resolution, which will be provided by the X-ray calorimeter X-IFU on board *Athena* will allow us to easily investigate the global X-ray properties of WISSH quasars with a modest amount of time.

We simulated a 0.2–10 keV X-IFU observation for a X-WISSH source with the lowest flux $f_{2-10} = 7 \times 10^{-15}$ erg s^{-1}cm^{-2} and with average redshift $z = 3.4$ (median for the whole WISSH sample), $\Gamma = 1.8$ and column density $N_H = 8 \times 10^{21}$ cm^{-2} (median for the X-WISSH sample). With this baseline spectral model, Athena/X-IFU can easily gather more than 600 counts in only 15 ks observation. This can give constraints on Γ and N_H at <10% and ~50% level (1σ error range), respectively.

Given the huge luminosity of the WISSH quasars, we expect these sources to be likely hosting widespread signs of outflows at all scales. Several theoretical models (King 2010; Faucher-Giguère & Quataert 2012; Zubovas & King 2012) propose that the kpc-scale outflows routinely observed in the ionized, neutral, and molecular phases are triggered by relativistic X-ray winds originating in the nuclear regions, the so-called ultra-fast outflows (UFOs; Tombesi et al. 2010). Recent observations lend support to this scenario, suggesting an energy-conserving expansion for the large-scale outflows (Feruglio et al. 2015; Tombesi et al. 2015).

Our WISSH sample is characterized by two distinct populations showing in UV and optical mildly ionized outflows in the nuclear region as large CIV blueshifts (≥2000 km s^{-1}; Vietri et al., in prep.) and at larger galaxy-wide scales as massive [OIII] outflows (≳2000 $M_\odot$ yr^{-1}; Bischetti et al. 2017). We can envisage a program to follow up these two categories and investigate the link between the UFOs and their outflow manifestations.

In order to simulate the spectral signatures from relativistic nuclear winds we used PHASE, which is a self-consistent photoionized absorber code (Krongold et al. 2003). Under the assumption of ionization balance, the code calculates the line opacity due to highly ionized metal transitions given (1) the equivalent hydrogen column density of ionized material (N_H^i); (2) ionization parameter U[7]; (3) turbulent velocity (v_{turb}); and (4) covering factor (f) of the photoionized plasma.

We simulated a Athena/X-IFU 15 ks observation for a baseline model with flux $f_{2-10} = 3 \times 10^{-14}$ erg s^{-1} cm^{-2}. This is the lowest flux for the subsample of sources for which we detect optical and UV signatures from mildly ionized outflows.

[7] $U = Q/4\pi r^2 cn$, where Q is the rate of hydrogen ionizing photons from a source at distance r, n is the hydrogen density, and c is the speed of light. The alternative ionization parameter ξ is defined as $\xi = L/nr^2$, where L is the isotropic luminosity ionizing source in the interval 13.6 eV to 13.6 keV.

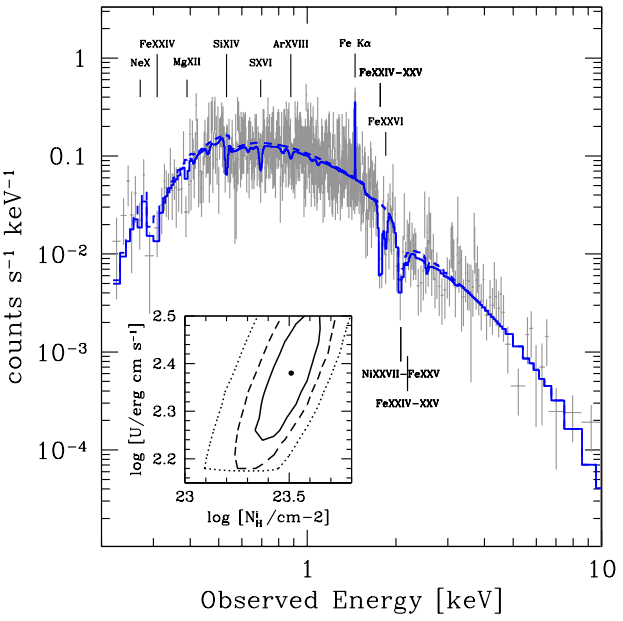

Fig. 14. Simulated Athena/X-IFU 15 ks spectrum for a WISSH-like quasar at $z = 3.4$ with UFO absorber with velocity $0.15c$, $N_H^i = 10^{23.4}$ cm^{-2}, $\log(U) = 2.3$, and $v_{turb} = 5000$ km s^{-1} (see Sect. 6.2). The solid line indicates the best-fit baseline continuum model modified by the UFO and the Fe Kα line (the dotted line indicates the baseline continuum component). Absorption lines with observed $EW > 1$ keV and the Fe Kα emission line are labeled. The inset shows confidence contours for U and $\log N_H^i$. Contours are 68, 90%, and 99% for two interesting parameters.

We modified this spectrum with PHASE assuming as physical parameters for the photoionized absorber those measured by Gofford et al. (2014) for the smallest detected feature (in their sequence 2013b) in the local WISSH analog PDS 456; i.e., one of the brightest $z < 0.2$ QSO ($L_{Bol} = 10^{47}$ erg s^{-1}), showing recurrent signatures of UFOs (Reeves et al. 2003, 2009, 2014). The parameters adopted are $N_H^i = 10^{23.4}$ cm^{-2}; $\log U = 2.3$, which roughly correspond to the estimated $\log[\xi/\mathrm{erg\,cm\,s^{-1}}] = 3.8$ in PDS 456, and $v_{turb} = 5000$ km s^{-1} (we assumed $f = 1$). To this model we added a narrow Fe Kα line with rest-frame equivalent width $EW = 100$ eV and intrinsic full width at half maximum of ~2000 km s^{-1} (Shu et al. 2010).

Figure 14 reports a simulated 15 ks X-IFU spectrum from an UFO with velocity $0.15c$. The 0.2–10 keV collected counts are ~2500. The solid line shows the best fit with the UFO signatures imprinted in the spectrum. The dotted model indicates the same best-fit model but without the absorption or emission line components. Constraints for $\log U$ and $\log N_H^i$ are reported in the inset. On average both parameters can be measured with an accuracy of ~5% and ~1%, respectively (90% c.l. for one interesting parameter). Such a level of accuracy is possible thanks to the presence of several highly ionized absorption lines arising in the 0.2–2 keV observed energy band (corresponding to rest frame 0.7–8 keV) from elements from OVIII to FeXXV–XXVI. This is clearly seen in Fig. 14. The most significant of these lines is the FeXXV at 6.7 keV, which is detected at ~10σ with an observed $EW = 800$ eV. The turbulent velocity of the UFO can be constrained with an accuracy of ~20%.

The EW of the Fe Kα line can be constrained with an accuracy of 25% and its position can be recovered at levels of 100–150 km s^{-1}, therefore allowing us to probe the kinematics of the

reflecting material (i.e., rotation of the accretion disk, bulk motion of outflowing material) down to such levels. This is crucial to obtain X-ray based redshift estimates competing with low-dispersion optical spectrographs and probe the dynamics of the quasar innermost regions by comparing it with the conditions of more external and lower ionization medium. These constraints allow us to accurately probe UFO properties in a sample of 20 WISSH quasars comprising 10 objects for each of the two WISSH subpopulations with a relatively modest investment of exposure time (300 ks). We can thus investigate the link between SMBH winds and kpc-scale outflows at extreme luminosity regimes and at the golden epoch of AGN-galaxy coevolution ($z \sim 2$–3). Thanks to the enormous leap in sensitivity of *Athena* compared to *Chandra* and *XMM-Newton* we can study the recurrence of these phenomena by probing their temporal variability on scales of few hours and start to investigate their (anti-)correlated variability with the enormous power radiated by the central engine as recently performed in a local less luminous AGN by Parker et al. (2017). In this way we will further probe how the integrated energy output injected into the ISM would affect the subsequent baryon cycle evolution in their host galaxy.

Acknowledgements. We thank the anonymous referee for helpful comments that improved the paper. We also acknowledge very useful discussions with B. Lusso. The scientific results reported in this article are based on observations made by the *Chandra* X-ray Observatory. We used observations obtained with *XMM-Newton*, an ESA science mission with instruments and contributions directly funded by ESA Member States and NASA. This work was supported by ASI/INAF contract I/009/10/0 and INAF PRIN 2011, 2012, and 2014. L.Z. acknowledges financial support under ASI/INAF contract I/037/12/0. M.B. and G.L. acknowledge support from the FP7 Career Integration Grant "eEASy": "supermassive black holes through cosmic time: from current surveys to eROSITA-Euclid Synergies" (CIG 321913). G.B. acknowledges financial support under the INTEGRAL ASI-INAF agreement 2013-025.R1. This research has made use of the NASA/IPAC Extragalactic Database (NED), which is operated by the Jet Propulsion Laboratory, California Institute of Technology, under contract with the National Aeronautics and Space Administration.

References

Avni, Y., & Tananbaum, H. 1982, ApJ, 262, L17
Banerji, M., Alaghband-Zadeh, S., Hewett, P. C., & McMahon, R. G. 2015, MNRAS, 447, 3368
Barger, A. J., Cowie, L. L., Capak, P., et al. 2003, AJ, 126, 632
Bianchi, S., Guainazzi, M., Matt, G., & Fonseca Bonilla, N. 2007, A&A, 467, L19
Bianchi, S., Maiolino, R., & Risaliti, G. 2012, Adv. Astron., 2012, 17
Bischetti, M., Piconcelli, E., Vietri, G., et al. 2017, A&A, 598, A122
Brandt, W. N., & Hasinger, G. 2005, ARA&A, 43, 827
Brandt, W. N., Laor, A., & Wills, B. J. 2000, ApJ, 528, 637
Brightman, M., Silverman, J. D., Mainieri, V., et al. 2013, MNRAS, 433, 2485
Bruni, G., Mack, K.-H., Salerno, E., et al. 2012, A&A, 542, A13
Carniani, S., Marconi, A., Maiolino, R., et al. 2015, A&A, 580, A102
Cash, W. 1979, ApJ, 228, 939
Chen, C.-T. J., Hickox, R. C., Goulding, A. D., et al. 2017, ApJ, 837, 145
Cicone, C., Maiolino, R., Sturm, E., et al. 2014, A&A, 562, A21
Civano, F., Elvis, M., Brusa, M., et al. 2012, ApJS, 201, 30
Coatman, L., Hewett, P. C., Banerji, M., et al. 2017, MNRAS, 465, 2120
Duras, F., Bongiorno, A., Piconcelli, E. 2017, A&A, 604, A67 (Paper II)
Del Moro, A., Alexander, D. M., Bauer, F. E., et al. 2016, MNRAS, 456, 2105
Faucher-Giguère, C.-A., & Quataert, E. 2012, MNRAS, 425, 605
Ferland, G. J., & Rees, M. J. 1988, ApJ, 332, 141
Feruglio, C., Bongiorno, A., Fiore, F., et al. 2014, A&A, 565, A91
Feruglio, C., Fiore, F., Carniani, S., et al. 2015, A&A, 583, A99
Fiore, F., Brusa, M., Cocchia, F., et al. 2003, A&A, 409, 79
Fiore, F., Puccetti, S., Brusa, M., et al. 2009, ApJ, 693, 447
Gallagher, S. C., Brandt, W. N., Chartas, G., & Garmire, G. P. 2002, ApJ, 567, 37
Gallagher, S. C., Richards, G. T., Hall, P. B., et al. 2005, AJ, 129, 567
Gehrels, N. 1986, ApJ, 303, 336
Gibson, R. R., Brandt, W. N., & Schneider, D. P. 2008, ApJ, 685, 773
Gofford, J., Reeves, J. N., Braito, V., et al. 2014, ApJ, 784, 77
Green, P. J., & Mathur, S. 1996, ApJ, 462, 637
Haardt, F., & Maraschi, L. 1991, ApJ, 380, L51
Haardt, F., & Maraschi, L. 1993, ApJ, 413, 507
Haardt, F., Maraschi, L., & Ghisellini, G. 1994, ApJ, 432, L95
Hall, P. B., Anderson, S. F., Strauss, M. A., et al. 2002, ApJS, 141, 267
Imanishi, M., & Terashima, Y. 2004, AJ, 127, 758
Jiang, Y.-F., Stone, J. M., & Davis, S. W. 2014, ApJ, 784, 169
Jiménez-Bailón, E., Piconcelli, E., Guainazzi, M., et al. 2005, A&A, 435, 449
Jin, C., Ward, M., & Done, C. 2012a, MNRAS, 425, 907
Jin, C., Ward, M., Done, C., & Gelbord, J. 2012b, MNRAS, 420, 1825
Just, D., Brandt, W., Shemmer, O., et al. 2007, ApJ, 665, 1004
Kaastra, J. S., Ebrero, J., Arav, N., et al. 2014, A&A, 570, A73
Kalberla, P., Burton, W., Hartmann, D., et al. 2005, A&A, 440, 775
Kelly, B. C., Bechtold, J., Trump, J. R., Vestergaard, M., & Siemiginowska, A. 2008, ApJS, 176, 355
King, A. R. 2010, MNRAS, 402, 1516
King, A. R., & Pounds, K. A. 2003, MNRAS, 345, 657
King, A., & Pounds, K. 2015, ARA&A, 53, 115
Korista, K., Baldwin, J., & Ferland, G. 1998, ApJ, 507, 24
Krawczyk, C. M., Richards, G. T., Mehta, S. S., et al. 2013, ApJS, 206, 4
Krongold, Y., Nicastro, F., Brickhouse, N. S., et al. 2003, ApJ, 597, 832
Kuraszkiewicz, J., Wilkes, B. J., Czerny, B., & Mathur, S. 2000, ApJ, 542, 692
La Franca, F., Fiore, F., Comastri, A., et al. 2005, ApJ, 635, 864
Lanzuisi, G., Piconcelli, E., Fiore, F., et al. 2009, A&A, 498, 67
Lanzuisi, G., Perna, M., Comastri, A., et al. 2016, A&A, 590, A77
Laor, A., & Brandt, W. 2002, ApJ, 569, 641
Laor, A., Fiore, F., Elvis, M., Wilkes, B. J., & McDowell, J. C. 1994, ApJ, 435, 611
Leighly, K. M. 2004, ApJ, 611, 125
Leighly, K. M., Halpern, J. P., Jenkins, E. B., et al. 2007, ApJ, 663, 103
Ludlam, R. M., Cackett, E. M., Gültekin, K., et al. 2015, MNRAS, 447, 2112
Luo, B., Brandt, W. N., Alexander, D. M., et al. 2013, ApJ, 772, 153
Luo, B., Brandt, W. N., Hall, P. B., et al. 2015, ApJ, 805, 122
Lusso, E., & Risaliti, G. 2016, ApJ, 819, 154
Lusso, E., Comastri, A., Vignali, C., et al. 2010, A&A, 512, A34
Lusso, E., Comastri, A., Simmons, B., et al. 2012, MNRAS, 425, 623
Lutz, D., Maiolino, R., Spoon, H. W. W., & Moorwood, A. F. M. 2004, A&A, 418, 465
Magdziarz, P., & Zdziarski, A. 1995, MNRAS, 273, 837
Maiolino, R., Marconi, A., Salvati, M., et al. 2001, A&A, 365, 28
Maiolino, R., Shemmer, O., Imanishi, M., et al. 2007, A&A, 468, 979
Marziani, P., Martínez Carballo, M. A., Sulentic, J. W., et al. 2016, Ap&SS, 361, 29
Mateos, S., Carrera, F., Alonso-Herrero, A., et al. 2015, MNRAS, 449, 1422
Mathur, S., Green, P. J., Arav, N., et al. 2000, ApJ, 533, L79
Matt, G., Perola, G. C., & Piro, L. 1991, A&A, 247, 25
Merloni, A., Predehl, P., Becker, W., et al. 2012, ArXiv e-prints [arXiv:1209.3114]
Miniutti, G., Fabian, A. C., Brandt, W. N., Gallo, L. C., & Boller, T. 2009a, MNRAS, 396, L85
Miniutti, G., Ponti, G., Greene, J. E., et al. 2009b, MNRAS, 394, 443
Murray, N., Chiang, J., Grossman, S. A., & Voit, G. M. 1995, ApJ, 451, 498
Nandra, K., George, I. M., Mushotzky, R. F., Turner, T. J., & Yaqoob, T. 1997, ApJ, 477, 602
Nandra, K., Le, T., George, I. M., et al. 2000, ApJ, 544, 734
Nandra, K., Barret, D., Barcons, X., et al. 2013, ArXiv e-prints [arXiv:1306.2307]
Nanni, R., Vignali, C., Gilli, R., Moretti, A., & Brandt, W. N. 2017, A&A, 603, A128
Page, K. L., Reeves, J. N., O'Brien, P. T., Turner, M. J. L., & Worrall, D. M. 2004, MNRAS, 353, 133
Parker, M. L., Pinto, C., Fabian, A. C., et al. 2017, Nature, 543, 83
Petrucci, P. O., Haardt, F., Maraschi, L., et al. 2000, ApJ, 540, 131
Petrucci, P.-O., Paltani, S., Malzac, J., et al. 2013, A&A, 549, A73
Piconcelli, E., Jimenez-Bailón, E., Guainazzi, M., et al. 2005, A&A, 432, 15
Piconcelli, E., Vignali, C., Bianchi, S., et al. 2015, A&A, 574, L9
Proga, D. 2003, ApJ, 585, 406
Proga, D. 2005, ApJ, 630, L9
Proga, D. 2007, in The Central Engine of Active Galactic Nuclei, eds. L. C. Ho, & J.-W. Wang, ASP Conf. Ser., 373, 267
Reeves, J. N., & Turner, M. J. L. 2000, MNRAS, 316, 234
Reeves, J. N., O'Brien, P. T., & Ward, M. J. 2003, ApJ, 593, L65
Reeves, J. N., O'Brien, P. T., Braito, V., et al. 2009, ApJ, 701, 493
Reeves, J. N., Braito, V., Gofford, J., et al. 2014, ApJ, 780, 45
Reis, R. C., & Miller, J. M. 2013, ApJ, 769, L7
Reynolds, C. S. 1997, MNRAS, 286, 513
Richards, G. T., Kruczek, N. E., Gallagher, S. C., et al. 2011, AJ, 141, 167

Runnoe, J. C., Brotherton, M. S., & Shang, Z. 2012a, MNRAS, 422, 478
Runnoe, J. C., Brotherton, M. S., & Shang, Z. 2012b, MNRAS, 426, 2677
Sabra, B. M., & Hamann, F. 2001, ApJ, 563, 555
Schartel, N., Rodríguez-Pascual, P. M., Santos-Lleó, M., et al. 2010, A&A, 512, A75
Shemmer, O., Brandt, W. N., Netzer, H., Maiolino, R., & Kaspi, S. 2008, ApJ, 682, 81
Shu, X. W., Yaqoob, T., & Wang, J. X. 2010, ApJS, 187, 581
Steffen, A. T., Strateva, I., Brandt, W. N., et al. 2006, AJ, 131, 2826
Stern, D. 2015, ApJ, 807, 129
Sturm, E., González-Alfonso, E., Veilleux, S., et al. 2011, ApJ, 733, L16
Teng, S. H., Brandt, W. N., Harrison, F. A., et al. 2014, ApJ, 785, 19
Tombesi, F., Cappi, M., Reeves, J. N., et al. 2010, A&A, 521, A57
Tombesi, F., Meléndez, M., Veilleux, S., et al. 2015, Nature, 519, 436
Treister, E., Krolik, J. H., & Dullemond, C. 2008, ApJ, 679, 140
Turner, T. J., & Miller, L. 2009, A&ARv, 17, 47
Vagnetti, F., Turriziani, S., Trevese, D., & Antonucci, M. 2010, A&A, 519, A17
Vanzella, E., Cristiani, S., Dickinson, M., et al. 2008, A&A, 478, 83
Vasudevan, R. V., & Fabian, A. C. 2007, MNRAS, 381, 1235
Vignali, C., Brandt, W. N., & Schneider, D. P. 2003, AJ, 125, 433
Vignali, C., Alexander, D. M., Gilli, R., & Pozzi, F. 2010, MNRAS, 404, 48
Weedman, D., Sargsyan, L., Lebouteiller, V., Houck, J., & Barry, D. 2012, ApJ, 761, 184
Wu, J., Brandt, W. N., Anderson, S. F., et al. 2012, ApJ, 747, 10
Xue, Y., Luo, B., Brandt, W., et al. 2011, ApJS, 195, 10
Young, M., Elvis, M., & Risaliti, G. 2009, ApJS, 183, 17
Zappacosta, L., Comastri, A., & Civano, F. 2017, ApJ, submitted
Zdziarski, A. A., Johnson, W. N., & Magdziarz, P. 1996, MNRAS, 283, 193
Zubovas, K., & King, A. 2012, ApJ, 745, L34

Appendix A: X-ray spectral properties of additional hyper-luminous quasars

We analyzed the *XMM-Newton* observations of three additional quasars that have redshift and bolometric luminosities comparable with those of WISSH objects, namely ULAS J1539+0557 (z = 2.658; Feruglio et al. 2014), ULAS J2315+0143 (z = 2.56; Banerji et al. 2015), and 2QZ 0028-2830 (z = 2.4; Shemmer et al. 2008). The X-ray data reduction and analysis were carried out following the same procedure outlined in Sects. 2.2 and 3.2, respectively. We can summarize the main results from the spectral analysis as follows:

– ULAS J1539+0557. This reddened quasar has a bolometric luminosity of $\mathrm{Log}[L_{\mathrm{Bol}}/\mathrm{erg\,s^{-1}}] = 48.2$ and a MIR luminosity $\mathrm{Log}[\lambda L_{6\,\mu\mathrm{m}}/\mathrm{erg\,s^{-1}}] = 47$, respectively (Feruglio et al. 2014). It was observed by *XMM-Newton* for ∼44.9 ks on 2015-02-16. The application of the PL model to the X-ray spectrum results into a very flat power law with $\Gamma \sim 1$. The addition of a rest-frame absorption component to the fitting model yields a significant improvement the quality of the fit (from Cstat/d.o.f. = 19/15 to 12/14). The best-fit value of the column density is $N_{\mathrm{H}} = 4.0^{+2.6}_{-1.7} \times 10^{22}\,\mathrm{cm^{-2}}$. The photon index derived by the APL model remains slightly flat ($\Gamma = 1.5^{+0.2}_{-0.2}$), but fixing Γ to the canonical value $\Gamma = 1.8$ results into a worsening of the fit. Using the APL model, we measured a hard X-ray flux of $f_{2-10} \sim 4 \times 10^{-14}\,\mathrm{erg\,cm^{-2}\,s^{-1}}$ and a luminosity of $\mathrm{Log}[L_{2-10}/\mathrm{erg\,s^{-1}}] = 45.1$.

– ULAS J2315+0143. This reddened quasar has a bolometric luminosity of $\mathrm{Log}[L/\mathrm{erg\,s^{-1}}] = 47.5$ (Banerji et al. 2015) and was targeted by *XMM-Newton* on 2014-12-16 for ∼55.9 ks. The X-ray spectrum is consistent with with a power law ($\Gamma = 1.64^{+0.09}_{-0.09}$) absorbed by a modest N_{H} of $0.7^{+0.4}_{-0.4} \times 10^{22}\,\mathrm{cm^{-2}}$. Fixing Γ to the canonical value of 1.8 does not significantly improve the quality of the fit. The hard X-ray flux and luminosity derived by the *XMM-Newton* spectrum fitted by the APL model are $f_{2-10} \sim 10^{-13}\,\mathrm{erg\,cm^{-2}\,s^{-1}}$ and $\mathrm{Log}[L_{2-10}/\mathrm{erg\,s^{-1}}] = 45.5$, respectively.

– 2QZ 0028-2830. This quasar was observed by *XMM-Newton* on 2009-12-07 for ∼22.2 ks. The PL model provides the best description for the X-ray spectrum. The resulting photon index is $\Gamma = 1.7^{+0.1}_{-0.1}$. The addition of an intrinsic absorber is not required by the fit, and only an upper limit on N_{H} can be inferred, i.e., $N_{\mathrm{H}} \leq 7.6 \times 10^{21}\,\mathrm{cm^{-2}}$. The hard X-ray flux of 2QZ0028−2830 is $f_{2-10} \sim 7 \times 10^{-14}\,\mathrm{erg\,cm^{-2}\,s^{-1}}$, which corresponds to a $\mathrm{Log}[L_{2-10}/\mathrm{erg\,s^{-1}}] \sim 45.3$. This quasar exhibits a bolometric luminosity of $\mathrm{Log}[L_{\mathrm{Bol}}/\mathrm{erg\,s^{-1}}] = 47.3$ (Carniani et al. 2015) and MIR luminosity of $\mathrm{Log}[\lambda L_{6\,\mu\mathrm{m}}/\mathrm{erg\,s^{-1}}] = 46.4$ derived by WISE photometric data.

Multiwavelength information about ULAS J1539+0557, ULAS J2315+0143 and 2QZ 0028-2830 are listed in Table A.1.

Table A.1. Summary of the multiwavelength properties of the three additional hyper-luminous quasars considered in this work.

Name	z	Γ	N_{H}	f_{2-10}	Log L_{2-10}	Log $\lambda L_{6\,\mu\mathrm{m}}$	Log L_{Bol}
(1)	(2)	(3)	(4)	(5)	(6)	(7)	(8)
ULASJ1539+0557	2.658	$1.5^{+0.2}_{-0.2}$	$4.0^{+2.6}_{-1.7}$	4.0	45.1	47.0	48.2
ULASJ2315+0143	2.56	$1.64^{+0.09}_{-0.09}$	$0.7^{+0.4}_{-0.4}$	9.2	45.5	47.5	47.5
2QZ0028-2830	2.4	$1.7^{+0.1}_{-0.1}$	≤0.76	6.8	45.3	46.4	47.3

Notes. Columns give the following information: (1) quasar ID; (2) redshift; (3) X-ray photon index; (4) absorption column densities N_{H} (in units of $10^{22}\,\mathrm{cm^{-2}}$); (5) 2–10 keV fluxes (in units of $10^{-14}\,\mathrm{erg\,cm^2\,s^{-1}}$); (6) 2–10 keV unabsorbed luminosities, (7) 6 μm luminosities, and (8) bolometric luminosities (in units of $\mathrm{Log}[L/\mathrm{erg\,s^{-1}}]$).